



On Detecting Nearby Nanohertz Gravitational Wave Sources via Pulsar Timing Arrays

Xiao Guo (郭潇)^{1,2}, Youjun Lu (陆由俊)^{1,2}, and Qingjuan Yu (于清娟)³¹ CAS Key laboratory for computational Astrophysics, National Astronomical Observatories, Chinese Academy of Sciences, 20A Datun Road, Beijing 100101, People's Republic of China; luyj@nao.cas.cn² School of Astronomy and Space Science, University of Chinese Academy of Sciences, 19A Yuquan Road, Beijing 100049, People's Republic of China³ Kavli Institute for Astronomy and Astrophysics and School of Physics, Peking University, Beijing 100871, People's Republic of China; yuqj@pku.edu.cn

Received 2022 January 13; revised 2022 September 9; accepted 2022 September 9; published 2022 November 2

Abstract

Massive binary black holes (MBBHs) in nearby galactic centers, if any, may be nanohertz gravitational wave (GW) sources for pulsar timing arrays (PTAs) to detect. Normally the objective GWs for PTA experiments are approximated as plane waves because their sources are presumably located far away. For nearby GW sources, however, this approximation may be inaccurate due to the curved GW wave front and the GW strength changes along the paths of PTA pulsar pulses. In this paper, we analyze the near-field effect in the PTA detection of nearby sources and find it is important if the source distance is less than a few tens of megaparsecs, and ignoring this effect may lead to a significant signal-to-noise underestimation especially when the source distance is comparable to the pulsar distances. As examples, we assume a nanohertz MBBH source located at either the Galactic Center (GC) or the Large Magellanic Cloud (LMC) according to the observational constraints/hints on the MBBH parameter space, and estimate its detectability by current/future PTAs. We find that the GC MBBH may be detectable by the Square Kilometer Array PTA. Detecting the LMC MBBH is challenging; however, if a number ($N \gtrsim 10$) of stable millisecond pulsars can be found in the LMC center, the MBBH may be detectable via a PTA formed by these pulsars. We further illustrate the near-field effects on the PTA detection of an isotropic GW background contributed mainly by nearby GW sources, and the resulting angular correlation is similar to the Hellings–Downs curve.

Unified Astronomy Thesaurus concepts: Black hole physics (159); Galactic center (565); Gravitational waves (678); Magellanic Clouds (990); Pulsars (1306); Supermassive black holes (1663)

1. Introduction

Pulsar Timing Arrays (PTAs) are aimed at detecting low-frequency gravitational waves (GWs) emitted from, e.g., massive binary black holes (MBBHs; Begelman et al. 1980; Yu 2002) and cosmic strings (e.g., Sazhin 1978; Detweiler 1979; Maggiore 2008; Sesana et al. 2009; Sesana & Vecchio 2010; Creighton & Anderson 2011; Sesana 2013; van Haasteren 2014; Blair et al. 2015; Mingarelli 2015; Taylor et al. 2019). Current PTAs include the Parkes PTA (PPTA; Manchester et al. 2013),⁴ the European PTA (EPTA; Kramer & Champion 2013),⁵ the North American Nanohertz Observatory for Gravitational Waves (NANOGrav; McLaughlin 2013; Ransom et al. 2019),⁶ the Indian Pulsar Timing Array (Joshi et al. 2018), and the Chinese pulsar timing array (CPTA). The first four combined together to form the International PTA (IPTA; Manchester & IPTA 2013; Perera et al. 2019).⁷ NANOGrav, PPTA, EPTA, and IPTA have all shown the existence of a signal from common-spectrum processes in the data, which might be due to the GW background (GWB) but lack significant evidence for quadrupolar spatial correlation (Arzoumanian et al. 2020; Chen et al. 2021a; Goncharov et al. 2021;

Antoniadis et al. 2022). This signal is possibly (partly) due to the ephemeris systematics and/or a single pulsar in the PTA data sets (Arzoumanian et al. 2021a). It was proposed to even be due to a non-Einsteinian polarization mode (scalar-transverse mode) signal (Chen et al. 2021b), but one should be cautious with the detailed data analysis; the probability for the existence of the scalar-transverse mode could be insignificant (Arzoumanian et al. 2021a). Nevertheless, this may suggest that the nanohertz GWB is close to being detected in the near future.

MBBHs with mass ratios $\gtrsim 0.01$ are predicted to exist in about a fraction of a few percent to 10% of nearby galaxies (Chen et al. 2020), some of which are also expected to be detected by PTAs in the future. These individual MBBHs (with distances at least many megaparsecs away; Sesana & Vecchio 2010; Deng & Finn 2011; Taylor et al. 2016; Schutz & Ma 2016; Perera et al. 2019; Arzoumanian et al. 2021b; Charisi et al. 2022) are usually much more distant than those of the stable millisecond pulsars (MSPs) in the Milky Way adopted in the PTAs (typically hundreds to ten thousands of parsecs away from the Earth; Manchester et al. 2005; Brazier et al. 2016). In this case, GWs emitted from an individual source can be regarded as plane waves in the data analysis as was done in many previous studies (e.g., Romano & Cornish 2017).

It has been proposed that MBBHs may even exist in our Galactic Center (GC), or some nearby galaxies, such as the Large Magellanic Cloud (LMC; e.g., Yu & Tremaine 2003; Portegies Zwart et al. 2006; Yu et al. 2007; Genzel et al. 2010; Tsuboi et al. 2017; Mingarelli et al. 2017; Girma & Loeb 2019; Takekawa et al. 2019; Arzoumanian et al. 2021b), which can

⁴ <http://www.atnf.csiro.au/research/pulsar/ppta/>⁵ <http://www.epta.eu.org/>⁶ <http://nanograv.org/>⁷ <http://www.ipta4gw.org/>

also be potential sources of future PTAs. However, these MBBHs are quite close to the Earth, with distances less than a few tens of kiloparsecs. Therefore, the conventional plane-wave assumption is probably inaccurate or even invalid when considering the detectability of these nearby MBBHs, if they exist, via PTAs (e.g., Deng & Finn 2011; Kocsis et al. 2012; McGrath & Creighton 2021). In this paper, we construct a general framework for studying the detectability of nanohertz GWs emitted from nearby MBBHs, if any, via PTAs, by considering that the propagation directions and amplitude of the GW from nearby sources are different at different locations along the path of pulses from a pulsar to the Earth (for comparison, see Maggiore 2008; Anholm et al. 2009; van Haasteren 2014; Mingarelli 2015; Taylor 2021, for distant GW sources).

Kocsis et al. (2012) discussed the problem of detecting a GW from a hypothetical MBBH in the GC. They mainly considered the case where all PTA pulsars were assumed to be located in the neighborhood of the GC. However, almost all known MSPs adopted in the current PTAs are not that close to the GC (Manchester & IPTA 2013; Brazier et al. 2016; Perera et al. 2019), and no MSP has been found in a direction close to the GC, yet (e.g., Manchester et al. 2005). Therefore, it is interesting to consider more realistic cases, in which MSPs adopted are the same as those adopted in current PTAs or similar to those expected from future surveys by the Five-hundred meter Aperture Spherical Telescope (Smits et al. 2009; Nan et al. 2011) and/or Square Kilometer Array (SKA; Lazio 2013; Wang & Mohanty 2017). In such a study, the GWs emitted from the hypothetical MBBHs cannot be approximated as plane waves because they are so close to PTA(s) and thus the “near-field” effect must be considered. Here the “near-field” effect refers to the effects of GWs from nearby sources by including both the curvature of the GW wave front and the change of the GW amplitude and phase along the paths of PTA pulsar pulses. It is worth noting that the definition of the “near-field” effect considered in Kocsis et al. (2012) is different from ours, which refer to the post-Newtonian effect (or Einstein delay) and tidal effects due to the MBBH on the motion of nearby pulsars (or Roemer delay), which were not considered in our paper for simplicity. Nevertheless, the PTA geometrical configuration considered in Kocsis et al. (2012) can be regarded as a special case of those in the present paper (see Appendix E).

McGrath & Creighton (2021) recently developed, for the first time, a Fresnel formalism to consider the nonplanar wave front for nearby GW sources, which is a treatment closer to the reality compared to the plane-wave approximation. For a nearby GW source, if any, even the Fresnel approximation is not sufficient. The reason for this is that the Fresnel formalism is still only valid under the far-field approximation, even though it improves the plane-wave approximation. In the present paper, we consider the accurate geometrical configuration without making those approximations and calculate the near-field effect for assumed nearby GW sources numerically, which is distinguished from that presented in McGrath & Creighton (2021).

This paper is organized as follows. We provide a general framework for considering the detectability of both nearby and distant nanohertz GW sources via PTAs in Section 2. Then we consider the cross-correlation between the signals from two MSPs in the near-field regime in Section 3 both for individual

sources and a GWB contributed mostly by nearby sources. Then we investigate detection strategies for PTAs (the matched-filtering and cross-correlation method) in Section 4 and calculate the influence of the near-field effect for PTA experiments in Section 5. In Section 6, we apply the framework to a hypothetical MBBH in the GC or nearby galaxies to calculate the signal-to-noise ratio (S/N) of the GWs emitted from these MBBHs. Conclusions and discussions are given in Section 7.

2. Perturbations on the Propagation of Pulses from Pulsars by the GWs from an MBBH

In this section, we introduce a general framework for calculating the redshift of frequency of pulses radiated from distant MSPs due to metric perturbations by GWs from distant sources. It can be reduced to the far-field approximation that is generally adopted in the PTA analysis.

2.1. General Framework

Figure 1 shows the schematic diagrams for PTA experiments with a single MSP, for both the general case (left diagram (a)) and the far-field approximation (right diagram (b)). In the general case, the distances of GW sources r could be comparable to, smaller than, or larger than distances of PTA MSPs L . This includes the near-field case where $r \lesssim L$. In the far-field approximation, the distances of GW targets are much larger than those of the PTA MSPs, and the GW radiation can be securely approximated as the plane wave (see diagram (b)).

The redshift of frequency ν of pulses from the MSP, received by an observer at time t_E , due to the perturbation of GWs can be expressed as (e.g., Anholm et al. 2009)

$$z(t_E) = \sum_a \int_0^L \mathcal{F}^a(l) \frac{dh_a|_Q}{dl} dl, \quad (1)$$

where $z(t_E) = (\nu(t_E) - \nu_0)/\nu_0$ represents the frequency shift, and the integral is from the Earth ($l = 0$) to MSP ($l = L$), ν_0 and $\nu(t_E)$ represent the received frequency of pulses without and with including GW induced redshift, respectively, $a = +, \times$, and the antenna pattern functions in the source frame

$$\mathcal{F}^+ = F^+ \cos 2\psi - F^\times \sin 2\psi, \quad (2)$$

$$\mathcal{F}^\times = F^+ \sin 2\psi + F^\times \cos 2\psi. \quad (3)$$

In the above equations, F^+ and F^\times are the antenna pattern functions for PTA in the detector frame, and ψ is the polarization angle (defined in Apostolatos et al. 1994; see Figure 1 therein), i.e., the rotation angle ($-\pi < \psi \leq \pi$) of the coordinate axis from a basis vector \hat{e}_1 to a principal reference direction in the source frame. Here \hat{e}_1 is defined to be the unit vector perpendicular to the pulsar-Earth-GW source plane, and the reference direction is defined as $\hat{n} \times \hat{\Omega}$ in the plane perpendicular to the GW propagation direction $\hat{\Omega}$, with \hat{n} representing the normal vector of the MBBH orbital plane. We also define a unit vector \hat{e}_2 , which is in the pulsar-Earth-GW source plane and perpendicular to $\hat{\Omega}$; thus, $(\hat{e}_1, \hat{e}_2, \hat{\Omega})$ can be taken as the basis vectors of a rectangular coordinate system. The inclination angle ι is defined as the angle between the GW propagation direction $\hat{\Omega}$ and \hat{n} (e.g., see Ellis et al. 2012; Babak & Sesana 2012; Zhu et al. 2014; Moore et al. 2015b; Zhu et al. 2015, 2016) and $\iota = \iota_E$ when $\hat{\Omega} = \hat{\Omega}_E$, L is the distance from

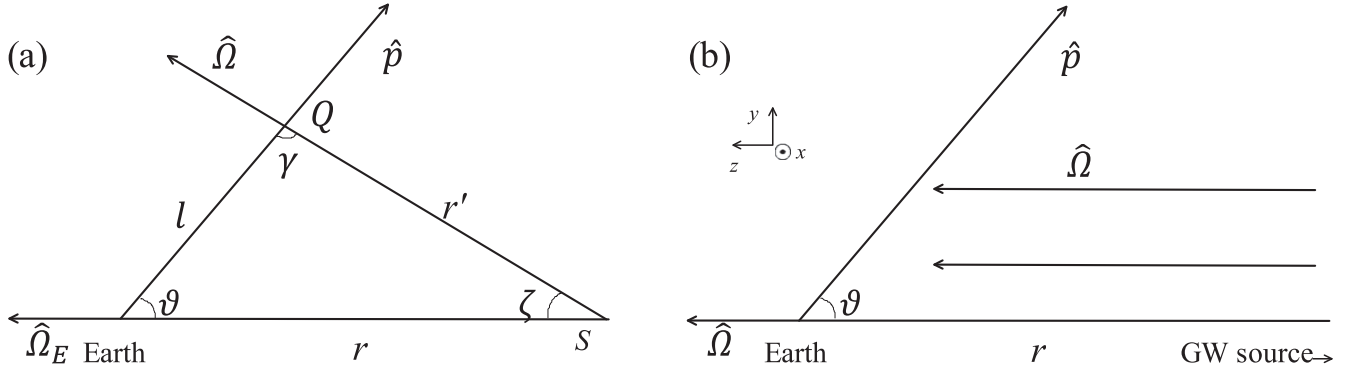


Figure 1. Schematic diagrams for PTA experiments with a single MSP (geometrical configuration). The left diagram (a) is for those cases that the distance from the target MSPs to Earth (L) is comparable to or not too much smaller than the distance of the GW source (point S) to Earth (r). The right diagram (b) is for those cases with $L \ll r$, in which the GW can be approximated as a plane wave. In diagram (a), Q denotes any point on the path of pulses from the MSP to Earth, l and r' denote the distance between Q and Earth, and between Q and GW source, respectively. γ , ζ , and ϑ represent the angles between GW propagation direction $\hat{\Omega}$ and that from Earth to MSP \hat{p} , between $\hat{\Omega}$ and that from GW source to Earth $\hat{\Omega}_E$, and between $-\hat{\Omega}_E$ and \hat{p} , respectively. In diagram (b), the GW propagation directions $\hat{\Omega}$ are assumed to be the same at different points Q . For the far-field regime, we adopt a Cartesian coordinate system shown at the top left of diagram (b), where the x -axis is perpendicular to the paper, and its positive direction \hat{e}_1 points toward us.

MSP to Earth, l is the distance between the Earth and point Q on the path from MSP to the Earth, and $h_a|_Q$ denotes the GW signal at point Q encoded in the pulsar pulses received by an observer at a given time t_E . For definitions of these relevant geometric quantities, see Figure 1.

For continuous GW, we have

$$h_+ = A_+ h_0 \cos \Phi(t), \quad (4)$$

$$h_\times = A_\times h_0 \sin \Phi(t), \quad (5)$$

where $h_0 = \frac{4G^{5/3} \mathcal{M}^{5/3} (\pi f)^{2/3}}{c^4 r}$, $A_+(\iota) = \frac{1 + \cos^2 \iota}{2}$, $A_\times(\iota) = \cos \iota$, \mathcal{M} is the chirp mass of this system, and $\Phi(t)$ is the phase of GW. For convenience, we put the dependence of the GW signal on ι out of $h_a|_Q$ (along with \mathcal{F}^a) rather than directly in $h_a|_Q$ in our following analysis. The antenna pattern functions are given by

$$F^+ = \frac{1}{2} \frac{\hat{p}^i \hat{p}^j}{1 + \hat{p} \cdot \hat{\Omega}} e_{ij}^+ = \frac{1}{2} \frac{(\hat{p} \cdot \hat{e}_1)^2 - (\hat{p} \cdot \hat{e}_2)^2}{1 + \hat{p} \cdot \hat{\Omega}}, \quad (6)$$

and

$$F^\times = \frac{1}{2} \frac{\hat{p}^i \hat{p}^j}{1 + \hat{p} \cdot \hat{\Omega}} e_{ij}^\times = \frac{(\hat{p} \cdot \hat{e}_1)(\hat{p} \cdot \hat{e}_2)}{1 + \hat{p} \cdot \hat{\Omega}}, \quad (7)$$

respectively, where \hat{p} is a unit vector pointing from the Earth to MSP, and \hat{p}^i and \hat{p}^j represent the components of \hat{p} with $i = 1, 2, j = 1, 2$. The components of the basis tensor \mathbf{e}^a are represented by e_{ij}^a , where

$$\mathbf{e}^+ = \hat{e}_1 \hat{e}_1 - \hat{e}_2 \hat{e}_2, \quad (8)$$

$$\mathbf{e}^\times = \hat{e}_1 \hat{e}_2 + \hat{e}_2 \hat{e}_1, \quad (9)$$

where

$$\hat{e}_1 = \frac{\hat{p} \times \hat{\Omega}}{|\hat{p} \times \hat{\Omega}|},$$

$$\hat{e}_2 = \hat{e}_1 \times \hat{\Omega}.$$

In the near-field regime, $\hat{\Omega}$ are different at different Q between the Earth and MSP, and the inclination and polarization angles (ι , ψ) vary with l significantly. Thus, the GW cannot be regarded as the plane wave in the near-field regime with L

comparable to or smaller than r . Hence \mathcal{F}^a is also a function of l ; thus, it cannot be separated from the integral, which is different from that adopting the far-field approximation (e.g., see Anholm et al. 2009).

We denote the phase of the GW received by an observer at time t_E as $\Phi_E(t_E)$. The phase of the GW at point Q ($\Phi|_Q$) encoded in pulsar pulses received by the observer at t_E is thus related to Φ_E due to the time delay $(l + r' - r)/c$ as

$$\Phi|_Q = \Phi_E \left(t_E - \frac{l + r' - r}{c} \right), \quad (10)$$

where r (r') is the distance between the GW source and Earth (Q point). Since amplitude $h_0(r) \propto 1/r$, we have

$$h_0|_Q = h_0 \left(t_E - \frac{l + r' - r}{c} \right) \bigg|_E \frac{r}{r'}. \quad (11)$$

Therefore, $h_a|_Q$ can be expressed in the inverse Fourier transform as

$$h_a|_Q = \frac{r A_a(\iota)}{r' A_a(\iota_E)} \int_{-\infty}^{\infty} df e^{i2\pi f (t_E - \frac{l+r'-r}{c})} \tilde{h}_a(f)|_E, \quad (12)$$

where $\tilde{h}_a(f)|_E$ is the strain spectrum of the GW signal $h_a(t_E)|_E$ at the Earth.

Combining Equations (12) and (1), the Fourier transform of the redshift is given by

$$\begin{aligned} \tilde{z}(f) &= \sum_a \frac{\tilde{h}_a(f)|_E}{A_a(\iota_E)} \int_0^L dl \mathcal{F}^a(l) \frac{d}{dl} \left(\frac{r A_a(\iota)}{r'} e^{-i2\pi f (\frac{l+r'-r}{c})} \right) \\ &\equiv \sum_a \mathcal{P}^a(f) \tilde{h}_{a,0}(f). \end{aligned} \quad (13)$$

In the above Equation, $\tilde{h}_a(f)|_E$ and $A_a(\iota_E)$ are independent of l , and the integral

$$\mathcal{P}^a(f) \equiv \int_0^L dl \mathcal{F}^a(l) \frac{d}{dl} \left(\frac{r A_a(\iota)}{r'} e^{-i2\pi f (\frac{l+r'-r}{c})} \right), \quad (14)$$

is integrated over l from 0 to L , $\frac{r A_a(\iota)}{r'} e^{-i2\pi f (\frac{l+r'-r}{c})}$ is a complex function of l , and its differential expression is too tedious to be explicitly shown here; $\mathcal{P}^a(f)$ represents the response of a PTA

pulsar to the GW signal, $\tilde{h}_{a,o}(f) \equiv \tilde{h}_a(f)|_E/A_a(\iota_E)$ equals the GW strain in the case with an optimal orientation ($\iota_E = 0$), and it is invariant for any $\iota_E (\neq 0)$. (For the expression of r' in the above equation, see Appendix B).

According to Equation (13), redshift $\tilde{z}(f)$ can be obtained given a known GW spectrum, distances (which can be measured accurately with timing parallax as proposed in Lee et al. 2011; see also D’Orazio & Loeb 2021), and directions to PTA pulsars, which suggests that the standard matched-filtering method (Maggiore 2008; Creighton & Anderson 2011; Moore et al. 2015a) can be adopted to extract GW signals and properties of GW systems. The optimum filter can be defined as $\tilde{z}(f)/S_n(f)$, with $S_n(f)$ describing the power spectrum density (PSD) of the noise for a given PTA. The S/N ϱ is then given by

$$\varrho^2 = \int_0^\infty df \frac{4|\tilde{z}(f)|^2}{S_n(f)}. \quad (15)$$

In the literature, for the detection of the GWB, it is straightforward to prove that (Hawking & Israel 1989; Maggiore 2008; Robson et al. 2019)

$$\overline{(\mathcal{F}^+)^2} = \overline{(\mathcal{F}^\times)^2}, \quad (16)$$

$$\overline{\mathcal{F}^+ \mathcal{F}^\times} = \overline{\mathcal{F}^\times \mathcal{F}^+} = 0. \quad (17)$$

The long overbar symbol $\overline{}$ in the above Equations represent the sky and polarization average defined by

$$\overline{X} \equiv \frac{1}{4\pi^2} \int_0^\pi d\psi_E \int d^2\hat{\Omega}_s X, \quad (18)$$

where $\hat{\Omega}_s$ represents the position of GW source.

For the detection of individual MBBHs, the position of the GW source is fixed, and the average should be taken over the sky for the directions of PTA MSPs ($\hat{\Omega}_p$). Note here that the cases for individual MBBHs and GWB are somewhat symmetric, which are an average over many pulsars (for a single source) and an average over many GW sources (background), respectively. According to the definition of $\mathcal{P}^a(f)$ in Equation (14), we have

$$\overline{\mathcal{P}^+ * \mathcal{P}^\times} = \overline{\mathcal{P}^\times * \mathcal{P}^+} = 0, \quad (19)$$

if the PTA MSPs are uniformly distributed. In the estimation of S/N, we define a mean quantity as

$$\chi^2 \equiv \frac{|\mathcal{P}^+|^2 + |\mathcal{P}^\times|^2}{2}, \quad (20)$$

which represents the geometrical effect of the spatial distribution of PTA pulsars relative to the GW propagation direction, and χ usually depends on ι_E and may also depend on L .⁸ We use $\bar{\chi}$ to represent the average of χ over ι_E in Section 5.3 (Equations (72) and (74)).

The rms value of the GW strain in the frequency domain is defined as (Gourgoulhon et al. 2019)

$$|\tilde{h}_o(f)|^2 \equiv |\tilde{h}_{+,o}(f)|^2 + |\tilde{h}_{\times,o}(f)|^2, \quad (21)$$

which is independent of ι_E , and then we have

$$|\tilde{z}(f)|^2 \approx \chi^2(f) |\tilde{h}_o(f)|^2. \quad (22)$$

The averaged S/N can thus be estimated as

$$\varrho^2 = \int_0^\infty df \frac{4\chi^2(f) |\tilde{h}_o(f)|^2}{S_n(f)}. \quad (23)$$

2.2. Reduction to the Far-field Approximation

Targets of nanohertz GWs are mostly inspiral MBBHs in galactic centers far away from the Earth and the distances from the Earth to those GW sources ($\gg 1$ Mpc) are much larger than the distances from the Earth to those MSPs (on the order of kiloparsecs) that are monitored by PTAs. Therefore, one may approximate the GWs emitted from those distant MBBHs as plane waves when considering its perturbation on the propagation of pulsar pulses to Earth.

If $r \gg L$, $\zeta \approx 0$, then $\hat{\Omega}$ and ι can be approximated as nonvariable constants $\hat{\Omega}_E$, ι_E , $r' = r - l \cos \vartheta$, $r'/r \approx 1$, $A_a(\iota)/A_a(\iota_E) \approx 1$. Therefore, Equation (13) can be reduced to

$$\begin{aligned} \tilde{z}(f) &= \sum_a \tilde{h}_a(f) \mathcal{F}^a \cdot (e^{-i2\pi f L(1-\cos \vartheta)/c} - 1) \\ &\equiv \sum_a \mathcal{P}_f^a(f) \tilde{h}_{a,o}(f), \end{aligned} \quad (24)$$

and

$$\mathcal{P}_f^a(f) = (e^{-i2\pi f L(1-\cos \vartheta)/c} - 1) \mathcal{F}^a A_a. \quad (25)$$

This is the expression resulting from the far-field approximation adopted in many previous works (e.g., Sazhin 1978; Detweiler 1979).

In the near-field regime, however, both the amplitudes and phases of GWs at different points Q may vary significantly, different from that in the case adopting the far-field approximation. The relative difference of GW amplitudes at r and r' is $[h_0(r) - h_0(r')]/h_0(r) = 1 - r/r' \lesssim 10^{-3}$ when $r > 10^3 L \sim O(\text{Mpc})$. Therefore, the amplitude difference is negligible if $r \gg 1$ Mpc. If the pulsar-to-Earth line is perpendicular to the Earth-to-GW source line, the difference between GW propagation direction at pulsar and that at Earth is the largest. The maximum distance difference between r' and r is then $|\sqrt{r^2 + L^2} - r| \sim L^2/2r$. If $L^2/2r \ll \lambda_{\text{GW}}/2$ (e.g., $\sim O(1 \text{ pc})$ for $f = 10^{-8}$ Hz), the phase difference can be ignored since it leads to a distortion of wave front much less than a half wavelength assuming pulsar distance on the order of kiloparsecs. Therefore, the phase difference can be nearly ignored as well if $r \gg 10$ Mpc. We conclude that the far-field approximation can be safely adopted if the distances of GW sources are much larger than 10 Mpc and the distances of PTA pulsars ~ 1 kpc, while the near-field effect must be considered if otherwise.

3. Cross-correlation of GW Signals

In the previous section, we considered the case of single MSP in the near-field regime. Below we consider the cross-correlations of GW signals in the time of arrival (TOA) data series of two MSPs for individual monochromatic GW sources (Section 3.1), nonmonochromatic individual GW sources (Section 3.2) in the near-field regime, and the near-field effect on the Hellings–Downs curve for a GWB (Section 3.3).

3.1. Individual Monochromatic GW Sources

The cross-correlation method can be also adopted to detect individual sources by two MSPs (or more) as an analogy to the method for the stochastic GWB (Hellings & Downs 1983;

⁸ In some literature, χ is denoted as the signal response function $\mathcal{R}(f)$.

Maggiore 2008; Anholm et al. 2009; Rosado et al. 2015; Taylor 2021). If

$$\langle \tilde{h}_{a,o}^*(f) \tilde{h}_{a',o}(f') \rangle = \frac{1}{2} \delta_{aa'} \delta(f - f') S_h(f) \quad (26)$$

can be applied to an individual source (e.g., individual monochromatic GW sources), where $\tilde{h}_a(f)$ and $\tilde{h}_{a'}(f')$ are the GW frequency spectra at the Earth encoded in the TOA data series of these two MSPs, respectively, $S_h(f)$ is the GW PSD, and $\langle \dots \rangle$ represents an ensemble average over many noise realizations (in reality, it can be replaced by a time average for a stationary stochastic noise). From Equation (13), we have

$$\begin{aligned} \langle \tilde{z}_1^*(f) \tilde{z}_2(f') \rangle &= \left\langle \sum_a \sum_{a'} \mathcal{P}_1^{*a}(f) \mathcal{P}_2^{a'}(f') \tilde{h}_{a,o}^*(f) \tilde{h}_{a',o}(f') \right\rangle \\ &= \frac{1}{2\beta_{12}} \delta(f - f') S_h(f) \Gamma_{12}(f), \end{aligned} \quad (27)$$

for two MSPs, where the overlap reduction function (ORF)⁹ in the near-field regime is defined as

$$\Gamma_{12}(f) \equiv \beta_{12} \sum_a \mathcal{P}_1^{*a}(f) \mathcal{P}_2^a(f), \quad (28)$$

and a normalization constant β_{12} is chosen for making $\Gamma_{12}(f) = 1$ for coincident coaligned detectors.

Similar to Anholm et al. (2009), the cross-correlation statistic can be defined as

$$S = \int_{-\infty}^{\infty} df \int_{-\infty}^{\infty} df' \delta_T(f - f') \tilde{s}_1^*(f) \tilde{s}_2(f') \tilde{Q}(f'), \quad (29)$$

where $\tilde{s}(f)$ is the Fourier transform of $s(t) = z(t) + n(t)$ with $n(t)$ representing the stochastic noise, and where $\tilde{Q}(f')$ is a filter, $\delta_T(f) = \sin(\pi f T) / (\pi f)$, and T is the observation time span. If the noise is stationary and Gaussian, then the mean of S is

$$\begin{aligned} \mu = \langle S \rangle &= \int_{-\infty}^{\infty} df \int_{-\infty}^{\infty} df' \delta_T(f - f') \langle \tilde{z}_1^*(f) \tilde{z}_2(f') \rangle \tilde{Q}(f') \\ &= \frac{T}{2\beta_{12}} \int_{-\infty}^{\infty} df S_h(f) \Gamma_{12}(|f|) \tilde{Q}(f). \end{aligned} \quad (30)$$

Assuming that the noise $n(t)$ is much greater than the signal $z(t)$, the variance is

$$\sigma^2 = \langle S^2 \rangle - \langle S \rangle^2 \approx \langle S^2 \rangle = \frac{T}{4} \int_{-\infty}^{\infty} df S_{n1}(f) S_{n2}(f) |\tilde{Q}(f)|^2, \quad (31)$$

where

$$\langle \tilde{n}_i^*(f) \tilde{n}_i(f') \rangle = \frac{1}{2} \delta(f - f') S_{ni}(f)$$

for $i = 1, 2$.¹⁰ Defining an inner product as

$$(A, B) \equiv \int_{-\infty}^{\infty} df A^*(f) B(f) S_{n1}(f) S_{n2}(f),$$

⁹ Here the ORF in Equation (28) is defined for individual sources, not for GWBs, to be discussed in Section 3.3.

¹⁰ According to the symmetry of Equations (26) and (3.1), $S_h(f)$ and $S_{ni}(f)$ must be real functions, $S_h(-f) = S_h^*(f) = S_h(f)$, and $S_{ni}(-f) = S_{ni}^*(f) = S_{ni}(f)$. However, $\Gamma_{12}(f)$ is a complex function, and $\Gamma_{12}(-f) = \Gamma_{12}^*(f) \neq \Gamma_{12}(f)$ in general.

then the mean and its variance can be rewritten as

$$\mu = \frac{T}{2\beta_{12}} \left(\tilde{Q}^*(f), \frac{S_h(f) \Gamma_{12}(|f|)}{S_{n1}(f) S_{n2}(f)} \right), \quad (32)$$

and

$$\sigma^2 \approx \frac{T}{4} (\tilde{Q}^*(f), \tilde{Q}^*(f)), \quad (33)$$

and the S/N is defined as

$$\varrho^2 = |\mu|^2 / \sigma^2. \quad (34)$$

According to the Schwartz inequality $|(A, B)|^2 \leq (A, A)(B, B)$, the optimum filter is

$$\tilde{Q}^*(f) = \frac{S_h(f) \Gamma_{12}(|f|)}{S_{n1}(f) S_{n2}(f)}, \quad (35)$$

and the maximum S/N is

$$\varrho^2 = \frac{T}{\beta_{12}^2} \left(\frac{S_h(f) \Gamma_{12}(|f|)}{S_{n1}(f) S_{n2}(f)}, \frac{S_h(f) \Gamma_{12}(|f|)}{S_{n1}(f) S_{n2}(f)} \right) \quad (36)$$

i.e.,

$$\varrho^2 = \frac{2T}{\beta_{12}^2} \int_0^\infty df \frac{S_h^2(f) \Gamma_{12}^2(|f|)}{S_{n1}(f) S_{n2}(f)}. \quad (37)$$

3.2. Individual Nonmonochromatic GW Sources

For individual nonmonochromatic GW sources (not satisfying Equation (26)), the mean of the cross-correlation statistics may be then generally defined as

$$\begin{aligned} \mu &\equiv \int_{-\infty}^{\infty} df \langle \tilde{z}_1^*(f) \tilde{z}_2(f) \rangle \tilde{Q}(f) \\ &= \left(\tilde{Q}^*(f), \frac{\langle \tilde{z}_1^*(f) \tilde{z}_2(f) \rangle}{S_{n1}(f) S_{n2}(f)} \right). \end{aligned} \quad (38)$$

Similarly, the optimum filter and the maximum S/N are given by

$$\tilde{Q}^*(f) = \frac{\langle \tilde{z}_1^*(f) \tilde{z}_2(f) \rangle}{S_{n1}(f) S_{n2}(f)}, \quad (39)$$

and

$$\varrho^2 = \frac{8}{T} \int_0^\infty df \frac{|\tilde{z}_1(f)|^2 |\tilde{z}_2(f)|^2}{S_{n1}(f) S_{n2}(f)}, \quad (40)$$

respectively, consistent with those given in Moore et al. (2015b). According to Equations (20), (21), and (27), the mean S/N can be roughly estimated as

$$\varrho^2 = \frac{8}{T} \int_0^\infty df \frac{\chi_1^2 \chi_2^2 |\tilde{h}_o(f)|^4}{S_{n1}(f) S_{n2}(f)}. \quad (41)$$

If the different polarization states of GW are independent from each other $\langle \tilde{h}_a^*(f) \tilde{h}_{a'}(f) \rangle = \delta_{aa'} \langle \tilde{h}_a^*(f) \tilde{h}_a(f) \rangle$, Equation (41) can be replaced by

$$\varrho^2 = \frac{8}{T \beta_{12}^2} \int_0^\infty df \frac{|\Gamma_{12}(f)|^2 |\tilde{h}_o(f)|^4}{S_{n1}(f) S_{n2}(f)}. \quad (42)$$

3.3. Near-field Effects on the Hellings–Downs Curve

In the traditional PTA data analysis for the GWB detection, it is assumed that the GWB is due to faraway GW sources, and the angular correlation between the responses of different pulsars to the GWB should provide critical evidence for the existence of such a GWB (if any; Hellings & Downs 1983; the so-called Hellings–Downs curve). If the GWB is mainly contributed by many nearby GW sources, one may think there might be some near-field effects on the detection of such a GWB, and in this case, the resulting angular correlation may be different from the Hellings–Downs curve. Below we estimate the near-field effect on the angular correlation between the responses of different PTA pulsars to the GWB, in addition to the main goal of the present paper, which is to consider the near-field effect for the PTA detection of individual sources.

The total redshift due to the GWB $z^b(t)$ can be expressed as the superposition of redshift $z(t, \hat{\Omega}_E)$ of many individual sources from all directions $\hat{\Omega}_E$, i.e.,

$$z^b(t) = \int d^2\hat{\Omega}_E z(t, \hat{\Omega}_E). \quad (43)$$

For a stationary, Gaussian, isotropic, unpolarized GWB, we have (Hellings & Downs 1983; Maggiore 2008; Anholm et al. 2009; Rosado et al. 2015; Taylor 2021)

$$\begin{aligned} \langle \tilde{h}_a^*(f, \hat{\Omega}_E) \tilde{h}_{a'}(f', \hat{\Omega}_E') \rangle &= \frac{1}{8\pi} \\ \delta(\hat{\Omega}_E - \hat{\Omega}_E') \delta_{aa'} \delta(f - f') S_h(f). \end{aligned} \quad (44)$$

Combining Equations (13) and (43), we obtain

$$\langle \tilde{z}_1^b(f) \tilde{z}_2^b(f') \rangle = \frac{1}{2\beta_{12}^b} \delta(f - f') S_h(f) \Gamma_{12}^b(f), \quad (45)$$

for two MSPs, i.e., 1 and 2. Here the ORF for the GWB in the near-field regime is defined as

$$\Gamma_{12}^b(f) \equiv \beta_{12}^b \int d^2\hat{\Omega}_E \sum_a \frac{\mathcal{P}_1^{*a}(f, \hat{\Omega}_E) \mathcal{P}_2^a(f, \hat{\Omega}_E)}{A_a^2(\iota_E)}, \quad (46)$$

and a normalization constant β_{12}^b is chosen to make $\Gamma_{12}^b(f) = 1$ for coincident coaligned detectors (two identical MSPs located at the same position). Some detailed formulas for the calculations of the ORF are listed in Appendix F. Different from the calculation of the ORF with the far-field approximation, the ORF in the near-field regime depends on the inclination angle ι_E , the pulsar distances L , and the sources' distances r . Since ι_E for GW sources may be randomly distributed, we can obtain the average ORF, i.e.,

$$\bar{\Gamma}_{12}^b(f) = \frac{\beta_{12}^b}{4\pi} \int d^2\hat{n} \int d^2\hat{\Omega}_E \sum_a \frac{\mathcal{P}_1^{*a}(f, \hat{\Omega}_E) \mathcal{P}_2^a(f, \hat{\Omega}_E)}{A_a^2(\iota_E)}, \quad (47)$$

by averaging over \hat{n} . Denoting the angle between two PTA MSPs as θ_{12} , $\bar{\Gamma}_{12}^b$ is a function of θ_{12} . To estimate $\bar{\Gamma}_{12}^b$ with consideration of the near-field effect, it needs to know the number distribution of the “nearby GW sources” as a function of r and the distances of PTA pulsars L . For simplicity, we assume that all of the “nearby GW sources” are located at the same distance to the observer (fixed r) and all of the PTA pulsars have the same L . In this way, $\bar{\Gamma}_{12}^b$ can be calculated for

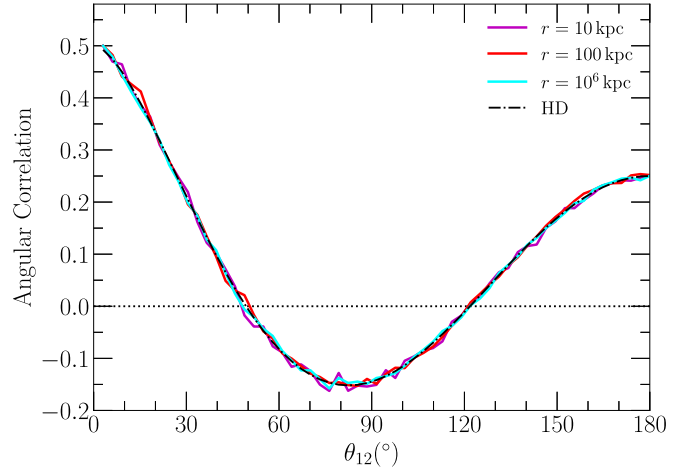


Figure 2. The angular correlation obtained by a PTA with all pulsars at distances of $L = 2$ kpc for a GWB due to nearby GW sources at a fixed distance of 10 kpc (magenta solid line), 100 kpc (red solid line), and 10^6 kpc (cyan solid line), respectively. The black dotted–dashed line shows the Hellings–Downs curve obtained by adopting the far-field approximation (Equation (48); Hellings & Downs 1983). Note here all of these curves are normalized to $1/2$ at $\theta_{12} \rightarrow 0^\circ$ as done for the Hellings–Downs (HD) curve (see Equation (48)).

each given set of r and L . We take $\bar{\Gamma}_{12}^b$ as the angular correlation function corresponding to the Hellings–Downs curve with considering the near-field effects.

Figure 2 illustrates the resulted $\bar{\Gamma}_{12}^b$ as a function of θ_{12} for $L = 2$ kpc, and $r = 10$ kpc (magenta solid line), 100 kpc (red solid line), and 10^6 kpc (cyan solid line), respectively. For comparison, we also show the standard Hellings–Downs curve obtained for a GWB contributed by faraway sources (black dotted–dashed line; Hellings & Downs 1983), with which the far-field approximation is suitable to be adopted, i.e.,

$$\bar{\Gamma}_{12}^b|_{r=\infty} = \frac{1}{2} - \frac{x}{8} + \frac{3}{4}x \ln \frac{x}{2}, \quad (48)$$

where $x = 1 - \cos \theta_{12}$ and $\bar{\Gamma}_{12}^b$ is renormalized to $1/2$ at $\theta_{12} \rightarrow 0^\circ$. We also renormalize those $\bar{\Gamma}_{12}^b$ obtained by limiting r to nearby sources to $1/2$ at $\theta_{12} \rightarrow 0^\circ$.¹¹ As seen from this figure, $\bar{\Gamma}_{12}^b$ in the near-field regime is similar to the standard Hellings–Downs curve obtained with the far-field approximation. This similarity can be understood by the following argument. Along the propagation path of the pulses from a pulsar to the observer, the metric perturbation due to the GWB should be uncorrelated with that at a different spacetime point along a different propagation direction of the pulses from another pulsar to the observer, if the distance of that point to the observer is much large than the GW wavelength. The contribution to the ORF comes mainly from the angular correlation of the effective metric perturbations at the same observer’s spacetime point (where the effective metric perturbation refers to the product of the metric perturbation and the pulsar antenna pattern function), similar to the case of the far-field approximation. That similarity also suggests that the near-field effect on the GWB S/N estimation is negligible.

¹¹ When $\theta_{12} = 0$, its value is one, but we do not show it in the figure and Equation (48). The unnormalized $\bar{\Gamma}_{12}^b$ values at $\theta_{12} \neq 0$ are basically consistent with each other.

We further note that the ORF value $\bar{\Gamma}_{12}^b(\theta)$ at $\theta_{12} = 0^\circ$ (not shown in Figure 2) in the near-field regime is different from that in the far-field regime. For example, the unnormalized value $\bar{\Gamma}_{12}^b(\theta = 0^\circ)/\beta_{12}^b$ is 1.64 (or 1.00) when the sources contributed to the GWB are all at $r = 3$ (or 8) kpc, while the unnormalized value $\bar{\Gamma}_{12}^b(\theta = 0^\circ)/\beta_{12}^b$ is two-thirds under the far-field approximation. This may indicate the difference between the near-field regime and the far-field regime.

Note also in the above analysis, the GWB from nearby sources is assumed to be isotropically distributed. One should be cautious about this assumption as a GWB produced by nearby sources may be anisotropic, and thus the analysis should be significantly different, which deserves further study.

4. Pulsar Timing Arrays

For a PTA with $N_p (\geq 3)$ MSPs, two different methods may be adopted to deal with data, which give different S/N estimates. Below we introduce the formulas for S/N estimates via the matched-filtering and the cross-correlation methods in Sections 4.1 and 4.2, respectively.

4.1. The Matched-filtering Method

Coherent network analysis has been developed for detecting individual sources via PTA (e.g., Ellis et al. 2012; Arzoumanian et al. 2014; Wang et al. 2014; Rosado et al. 2015; Wang et al. 2015), which is similar to that for the network of ground-based GW detectors (Jaranowski et al. 1996). For the TOA data from each MSP, the standard matched-filtering method can be used to estimate S/N. With this method, the total S/N obtained from the PTA observations can be given by (see Section 2.1)

$$\varrho^2 = \sum_{i=1}^{N_p} \int_0^\infty df \frac{4\chi^2(f)|\tilde{h}_o(f)|^2}{S_{ni}(f)}, \quad (49)$$

where the summation is over all N_p MSPs. For convenience, the total S/N used for theoretical analysis may be approximated as

$$\varrho^2 \simeq N_p \int_0^\infty df \frac{4\chi^2(f)|\tilde{h}_o(f)|^2}{S_n(f)}, \quad (50)$$

by assuming that all MSPs contribute to the S/N equally (see also Moore et al. 2015b).

The S/N estimate given by the above Equation (50) can be treated as an effective S/N, though the real S/N for a PTA observations can be obtained only by considering the detailed properties of each MSP adopted in the PTA. For example, the effective S/N was adopted in Moore et al. (2015b), Huerta et al. (2015), and Thrane & Romano (2013), to estimate sensitivity curves for PTAs. In reality, different MSPs adopted in the PTA may have quite different properties and thus contribute to the S/N differently. The contributions to the S/N may be led by several close-to-source MSPs with small timing rms noise. Therefore, more careful estimation of the S/N should consider the properties of each MSP adopted in the PTA observations.

4.2. The Cross-correlation Method

The cross-correlation method has also been introduced for detecting individual sources via PTA, similarly to that for the detection of a stochastic GWB (Maggiore 2008; Moore

et al. 2015b), particularly when the redshift $z(f)$ is difficult to obtain. According to Section 3, the S/N estimated from the cross-correlation method for any two PTA MSPs (i, j , and $i \neq j$) is

$$\varrho_{ij}^2 = \frac{2T}{\beta_{ij}^2} \int_0^\infty df \frac{S_h^2(f)|\Gamma_{ij}(f)|^2}{S_{ni}(f)S_{nj}(f)} \quad (51)$$

or

$$\varrho_{ij}^2 = \frac{8}{T} \int_0^\infty df \frac{\chi_i^2 \chi_j^2 |\tilde{h}_o(f)|^4}{S_{ni}(f)S_{nj}(f)}. \quad (52)$$

In Equation (51), the ORF of the i - and j -MSPs is defined as

$$\Gamma_{ij}(f) \equiv \beta_{ij} \sum_a \mathcal{P}_i^{*a}(f) \mathcal{P}_j^a(f), \quad (53)$$

where β_{ij} is adopted to make $\Gamma_{ij}(f) = 1$ for coincident coaligned detectors (see also Equation (28) for Γ_{12}). The total S/N is the summation of ϱ_{ij} over all MSP pairs, i.e., (Maggiore 2008; Moore et al. 2015b)

$$\varrho^2 = \sum_{i=2}^{N_p} \sum_{j=1}^{i-1} \varrho_{ij}^2. \quad (54)$$

If also assuming that different MSPs contribute equally, the total S/N can be roughly estimated as

$$\varrho^2 = \frac{4N_p(N_p - 1)}{T} \int_0^\infty df \frac{\chi^4 |\tilde{h}_o(f)|^4}{S_n^2(f)}. \quad (55)$$

5. The Near-field Effect

In this Section, we compare the differences of some characteristic quantities in the cases adopting the far-field approximation from that in the general framework by including the near-field effect. We then estimate the values of χ for some example systems in these two cases, of which the difference mainly represents the importance of the near-field effect on average.

5.1. The Function $\mathcal{P}^a(f)$

We first analyze the function $\mathcal{P}^a(f)$ in both the far-field and near-field regimes in some special cases to illustrate their differences.

5.1.1. The Far-field Approximation

If denoting $\Delta\Phi$ as $\Delta\Phi = -2\pi fL(1 - \cos\vartheta)/c$, then $e^{i\Delta\Phi} - 1 = 2\sin(\Delta\Phi/2)e^{i(\Delta\Phi/2+\pi/2)}$. According to Equation (25), we have the far-field approximation of $\mathcal{P}^a(f)$ as

$$\mathcal{P}_f^a(f) = 2\sin\left(\frac{\Delta\Phi}{2}\right)e^{i(\Delta\Phi/2+\pi/2)}\mathcal{F}^a. \quad (56)$$

If $L \sim 1$ kpc, $f \sim 10^{-8}$ Hz, then $fL/c \sim 10^3 \gg 1$, and the exponential factor oscillates with frequency f rapidly. Hence $|\mathcal{P}_f^a(f)|$ also oscillates with f in the range $[0, 2\mathcal{F}^a]$ rapidly, and the average of its absolute value is $|\overline{\mathcal{P}_f^a(f)}| = \sqrt{2}\mathcal{F}^a$. This oscillation of $\mathcal{P}^a(f)$ modulates the waveform detected by the PTA, and thus it should be carefully considered in the S/N estimates.

An example is provided below to show how to calculate \mathcal{F}^a . We define a coordinate system, in which the GW source is

located at the negative direction of z -axis, and PTA pulsars are located in the yOz plane (see Figure 1(b)). In this coordinate system, $\hat{\Omega} = (0, 0, 1)$, $\hat{p} = (0, \sin \vartheta, -\cos \vartheta)$ if adopting the far-field approximation. According to Equations (6) and (7), one should have

$$F^+ = -\frac{\sin^2 \vartheta}{2(1 - \cos \vartheta)} = -\frac{1 + \cos \vartheta}{2}, \quad (57)$$

$$F^\times = 0, \quad (58)$$

and also

$$|\mathcal{P}_f^+(f)| \propto (1 + \cos \vartheta) \left| \sin \left(\frac{\Delta \Phi}{2} \right) \right|, \quad (59)$$

$$|\mathcal{P}_f^+(f)| = 0. \quad (60)$$

This result is consistent with that derived in Lee et al. (2011). Furthermore, if the inclination angle $\iota = 0$ and polarization angle $\psi = 0$, then

$$|\mathcal{P}_f^+(f)| = (1 + \cos \vartheta) \left| \sin \left(\frac{\Delta \Phi}{2} \right) \right|. \quad (61)$$

5.1.2. The Near-field Regime

In this near-field regime, we define a coordinate system $(\hat{e}_1, \hat{e}_2, \hat{\Omega})$ (see Appendix A), which rotates with GW propagation direction to make $\hat{\Omega} = (0, 0, 1)$ even for different l , and $\hat{p} = (0, \sin \gamma, \cos \gamma)$. The inclination angle ζ changes along the path of pulsar pulses. In this case, $\mathcal{P}^a(f)$ can be calculated numerically (for details, see Appendix B and Figure 1(a)) and it also oscillates with f , similar to that shown for the case adopting the far-field approximation. To illustrate the behavior of $\mathcal{P}^a(f)$ as a function of frequency, we assume $\vartheta = \pi/2$, $L = 1$ kpc, and $r = 8$ kpc (i.e., a source at the GC), $\iota_E = \psi_E = 0$; thus, $\mathcal{P}^+(f) \neq 0$ and $\mathcal{P}^\times(f) = 0$. For these settings, we adopt both the far-field approximation as described in Section 5.1.1 and the general formulas that include the near-field effect to calculate $\mathcal{P}_f^a(f)$ and $\mathcal{P}_f^+(f)$, respectively. Figure 3 shows the relative difference between $\mathcal{P}_f^+(f)$ and $\mathcal{P}^+(f)$, which is significant at a large fraction of frequencies.

The quantity $\mathcal{P}^a(f)$ also depends on the relative angle between the directions of MSP and GW source ϑ . Figure 4 illustrates such an angular dependence for two assumed nearby GW sources in a plane of ρ versus ϑ . Here ρ represents the absolute value of $\mathcal{P}^+(f)$. The red solid line represents the envelope curve of $|\mathcal{P}_f^+(f)|$ by adopting the far-field approximation, i.e., $\rho = 1 + \cos \vartheta$, which is consistent with that studied in Lee et al. (2011) for the response pattern of distant sources. The red dashed line represents the curve $\rho = \rho_0(1 + \cos \vartheta)$ with $\rho_0 = \max(|\mathcal{P}^+(f)|)$, which has a similar shape to the red solid line. As seen from this Figure, the near-field effect leads to the shape distortion of $|\mathcal{P}^+(f)|$ dependent on ϑ . There are small white empty areas around $\rho = 0$ in both panels of Figure 4, different from those shown for the case adopting far-field approximation in Lee et al. (2011). The reason for this is as follows. If the far-field approximation is valid, the amplitude and propagation direction of GWs are almost the same at different Q on the path of pulses, respectively, and only the GW phases are different at different Q . At phases $2\pi n$ (n is an integer), $\mathcal{P}_f^a(f)$ vanishes even $\mathcal{P}^a \neq 0$, as indicated by Equation (25). However, in the near-field regime, the GWs from the same source have different

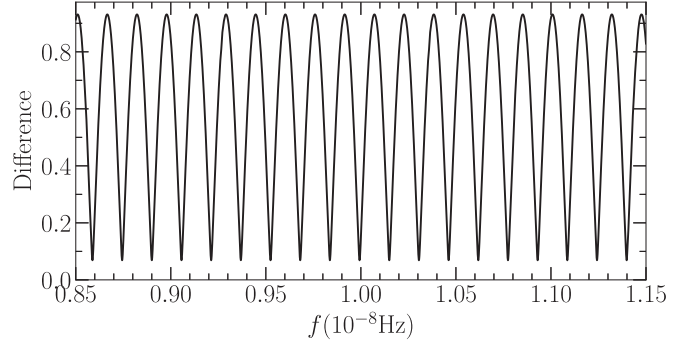


Figure 3. Relative difference of $\mathcal{P}^+(f)$ resulting from the near-field regime and that from the far-field approximation at different frequencies, defined as $|\mathcal{P}^+(f) - \mathcal{P}_f^+(f)| / \max(|\mathcal{P}_f^+(f)|)$. The GW source is assumed to be located at $r = 8$ kpc and the pulsar distance is assumed to be $L = 1$ kpc. This figure illustrates that the near-field effect is important at almost all frequencies. See details in Section 5.1.2.

directions, amplitudes, and phases, at different Q on the path of pulses. The superposition of the GW effect at different parts of the path generally does not vanish, and thus $\mathcal{P}^a(f)$ is oscillating but cannot reach zero, as shown in Figure 4.

The small-scale spiky features (Figure 4) may enable precise localization of GW sources via PTA observations, if pulsar distances can be measured accurately by the timing parallax and the curvature of GW wave front (Deng & Finn 2011) or some other methods with an error not larger than the GW wavelength (see Lee et al. 2011). The angular dependence is much different from the dependence on the frequency or pulsar distance; therefore, they can be distinguished. In principle, it is plausible that timing parallax can give accurate distance measurements for pulsars. In observations, however, pulsar distances may be difficult to be measured via timing parallax with an accuracy $\ll 0.1\%$, and the GW radiation may be not strictly monochromatic (due to the finite observation time span T). Thus, f and L are degenerate with each other in the case adopting the far-field approximation. However, the degeneracy between f and L may be broken in the near-field regime since $\mathcal{P}^a(f)$ is not strictly periodic. The spiky features in the response of PTA can also help to locate the angular position of a GW source within a lobe as these spiky lobes form many concentric circles in the sky and the intersection of the concentric circles of many PTA pulsars gives the source position (Lee et al. 2011). From Figure 4 (left-bottom subpanel), we can see that the width of each lobe is $\lesssim 1^\circ$; thus, the location of the GW source at $r = 8$ kpc may be identified with an accuracy of 1° . However, the precision may be significantly decreased because of the nonzero noises in the actual observations.

It is therefore important to adopt the general formalism presented in Section 2.1 when considering the detection of nearby GW sources by PTAs, as adopting the (inaccurate) far-field approximation in such cases would introduce significant errors in the waveform templates (as the production of $\mathcal{P}_f^a(f)$ and $\tilde{h}(f)$; for an example, see Figure 8 below) and thus in the parameter estimates.

If inaccurate GW templates are used to match, then it leads to a decline of S/N or incorrect parameter estimations. Such an effect can be described by the fitting factor (FF) defined as (Ajith et al. 2008)

$$\text{FF} \equiv \frac{\{s|h\}}{\sqrt{\{s|s\}\{h|h\}}}, \quad (62)$$

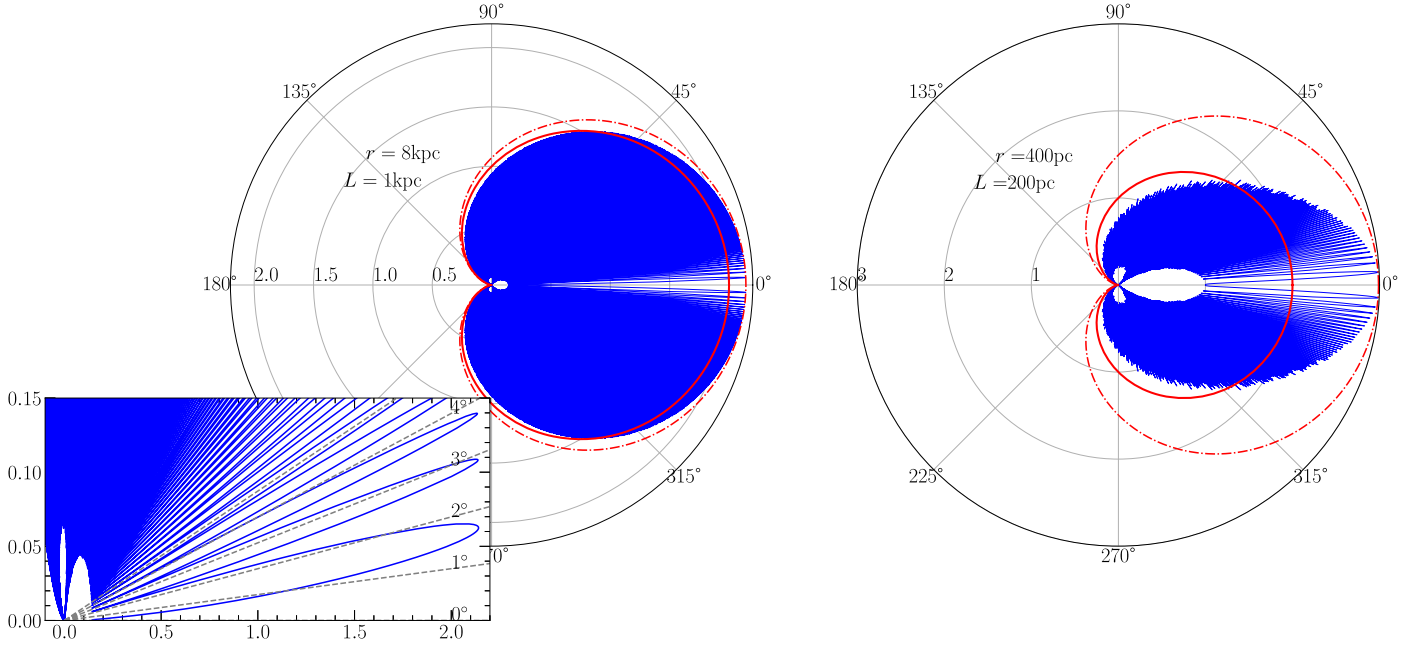


Figure 4. $|\mathcal{P}^+(f)|$ as a function of ϑ (Equations (14) and (B1)). Left panel: the GW source is located at $r = 8$ kpc (e.g., at the GC) and the pulsar distance is $L = 1$ kpc; a subpanel at the left-bottom corner shows the detail of the pattern, and we use several gray dashed lines to represent the 1° mesh grid. Right panel: $r = 400$ pc, $L = 200$ pc, $f = 10^{-8}$ Hz, and $t_E = 0$. The red solid line represents the envelope curve of $|\mathcal{P}^+(f)|$ obtained by adopting the far-field approximation, i.e., $\rho = 1 + \cos \vartheta$. The red dashed line represents $\rho = \rho_0(1 + \cos \vartheta)$ with $\rho_0 = \max(|\mathcal{P}^+(f)|)$ representing the maximum value of $|\mathcal{P}^+(f)|$ over ϑ in the range from 0 to 2π . The near-field effect is clearly shown by the difference between the red solid curve and the outer envelope of the blue curve. The rapid oscillation of $|\mathcal{P}^+(f)|$ with ϑ may suggest a high angular resolution for the detection of individual GW sources. The right panel shown here is only for illustrative purpose. See details in Section 5.1.2.

where s is the actual signal, h is the template, and $\{\cdot|\cdot\}$ represents the inner product defined as

$$\{s|h\} \equiv 4\Re\left(\int_0^\infty \frac{\tilde{s}^*(f)\tilde{h}(f)}{S_n(f)}df\right), \quad (63)$$

and $\Re(Z)$ represents the real part of Z . When $s = h$, we obtain the optimal S/N, i.e., $\varrho_{\text{opt}} = \sqrt{\{s|s\}}$, while if h is close to s , but not equal to s , we obtain the actual S/N with template h as $\varrho = \sqrt{\{s|h\}} \simeq \sqrt{\text{FF}} \varrho_{\text{opt}}$.

In our example, we regard the accurate waveform in the near field (at distance r) as s , and regard the waveform in the far-field approximation as h . We can then define a threshold for FF (FFS) as

$$\text{FFS} \equiv 1 - \frac{1}{2\varrho_{\text{th}}^2} \quad (64)$$

to show the significance of the near-field effect (see Lindblom et al. 2008; Fang et al. 2019).¹² This criterion is $\text{FFS} = 0.944$ when adopting a threshold of S/N as $\varrho_{\text{th}} = 3$, and 0.995 when adopting $\varrho_{\text{th}} = 10$, respectively. As an example, we calculate the FF of the templates resulting from the far-field approximation and those after considering the near-field effect, respectively. In reality, each pulsar in a PTA has a different direction and distance that leads to different waveform to match in the near-field regime. To clearly show the dependence of FF (or $\delta\hat{\varrho}$, whose definition can be seen from Equation (65) at the end of this subsection) on each variable, for simplicity, we assume the same GW waveform is adopted to calculate the FF (or $\delta\hat{\varrho}$) for all PTA pulsars. According

to Equation (62), we obtain $\text{FF} = 0.54$ for a monochromatic GW signal with $h_0 = 10^{-15}$ and $f = 10^{-8}$ Hz from the GC, monitored by the SKA-PTA with the properties listed in Table 1 (for simplicity, we set $L = 1$ kpc). This small FF value means that the adoption of inaccurate templates under the far-field approximation, without considering the near-field effect, leads to a significant S/N decline (e.g., by a factor of 1.36 for the above case) and a less good match.

Figure 5 (top panel) shows FF for those GW sources with similar properties but located at different distances r , monitored by a PTA with MSPs at $L = 2$ kpc or $L = 10$ kpc. It is clear that the near-field effect is important at least for GW sources at $r \lesssim$ a few megaparsecs, and it should be considered when considering the detectability and extracting the GW signal of nearby sources in the PTA data. For different parameter settings (e.g., ϑ), the results may be quantitatively different, but we can still obtain similar near-field effects qualitatively (as seen in Appendix D). We defer a more comprehensive investigation of the errors in the parameter estimates induced by ignoring the near-field effect to future work.

If the difference between waveform s and h is significant, i.e., $s \sim h$ is incorrect, we can describe the difference of s and h by a relative quantity as (Guo & Lu 2022)

$$\delta\hat{\varrho} \equiv \sqrt{\frac{\{s-h|s-h\}}{\{s|s\}}}. \quad (65)$$

When $s \equiv h$, $\delta\hat{\varrho} = 0$. Figure 5 also shows $\delta\hat{\varrho}$ as the function of source distance r (bottom panel). The larger $\delta\hat{\varrho}$ is, the larger the difference between s and h . Despite the differences in the definitions of FFS and $\delta\hat{\varrho}$, they give similar results on the significance of the near-field effect as a function the GW source distance (top and bottom panels).

¹² Note that this threshold FF is valid only when $s \simeq h$. If the difference between s and h is too large, this criterion would be invalid.

Table 1

Estimated S/N Values for Hypothetical GW Sources at Different Frequencies Monitored by Current, Future, and Hypothetical PTAs with Assumed Properties by Using Different S/N Estimation Methods

PTAs	N_p	σ (ns)	T (yr)	Δt (yr)	r_p (pc)	M_{\bullet} (M_{\odot})	q	Location	S/N _{MF} (f)			S/N _{CC} (f)		
Single PTA	20	100	20	0.04	...	$4.26 \cdot 10^6$	0.01	GC	0.41	0.31	0.21	0.08	0.05	0.02
IPTA	49	100	20	0.04	...	$4.26 \cdot 10^6$	0.01	GC	0.64	0.49	0.33	0.20	0.12	0.05
IPTA ^{opt}	200	30	20	0.01	...	$4.26 \cdot 10^6$	0.01	GC	3.09	6.32	4.38	4.77	19.9	9.55
CPTA	100	20	20	0.04	...	$4.26 \cdot 10^6$	0.01	GC	2.10	3.40	2.32	2.19	5.75	2.64
SKA	10^3	10	20	0.04	...	$4.26 \cdot 10^6$	0.01	GC	7.13	20.4	14.7	25.4	207.3	107.6
SKA ^{opt}	10^3	10	20	0.01	...	$4.26 \cdot 10^6$	0.001	GC	0.74	3.49	2.98	0.27	6.08	4.45
GC-PTA	10	100	20	0.02	1	$4.26 \cdot 10^6$	0.0001	GC	21.8	17.7	11.9	226	149	67.0
LMCC-PTA1	20	100	10	0.02	1	$2.4 \cdot 10^4$	0.1	LMC	3.70	4.55	2.48	6.65	10.1	2.99
LMCC-PTA2	5	100	10	0.02	0.1	$2.4 \cdot 10^4$	0.1	LMC	18.5	22.8	12.4	153	232	68.6

Note The columns from left to right list the name of the PTAs, number of pulsars (N_p), pulsar timing precision (σ) in units of nanoseconds, total observational period T_{obs} in units of years, time interval for each observation Δt in units of years, distance of the pulsar to the GW source r_p in units of parsecs, total MBBH mass M_{\bullet} in units of solar mass, mass ratio q , location of the GW source, estimated S/N values for those GW sources at frequency $f = 10^{-8}$, 3×10^{-8} , and 10^{-7} Hz, by the matched-filtering method (MF) and the cross-correlation method (CC), respectively.

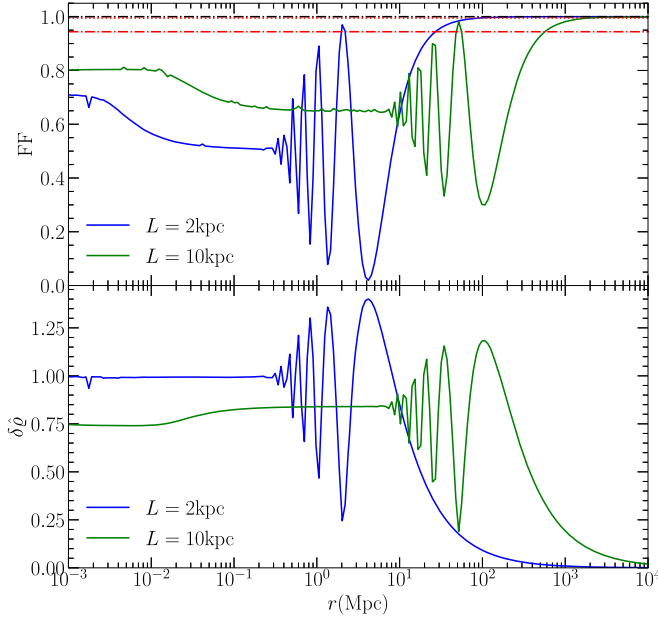


Figure 5. Top panel: FF as a function of the GW source distance (Equation (62)) obtained by adopting the far-field approximation. Bottom panel: $\delta\hat{\Theta}$ as a function of the GW source distance (Equation (65)) obtained by adopting the far-field approximation. The MSP is assumed to be at $L = 2$ kpc (blue) or $L = 10$ kpc (green) with $\vartheta = \frac{\pi}{2}$. This figure shows that near-field effect can be significant for $L = 2$ kpc (10 kpc) when the GW source distance $r \lesssim 27$ Mpc (572 Mpc) or $\lesssim 91$ Mpc (1.9 Gpc), with corresponding FF $\gtrsim 0.944$ (indicated by the red dotted-dashed line in top panel) or $\gtrsim 0.995$ (indicated by the red dotted line in top panel), if the S/N threshold is set to be 3 or 10. In the top panels, the black dotted-dashed lines represent FF = 1.

5.2. Overlap Reduction Function $\Gamma_{12}(f)$ for Individual Sources

In this subsection, we show the difference of ORF between far-field approximation and the near-field regime.

5.2.1. The Far-field Approximation

According to Equation (28), the absolute value of ORF is given by

$$|\Gamma_{12}(f)| = \left| \beta_{12} \sum_a \mathcal{P}_1^{*a}(f) \mathcal{P}_2^a(f) \right|. \quad (66)$$

For simplicity, we calculate the ORF values in a case assuming that two MSPs are located in different directions (ϑ) but the same plane (e.g., yOz , see Figure 1).¹³ For such a setting,

$$|\Gamma(f)| \propto (1 + \cos \vartheta_1)(1 + \cos \vartheta_2) \left| \sin\left(\frac{\Delta\Phi_1}{2}\right) \sin\left(\frac{\Delta\Phi_2}{2}\right) \right|, \quad (67)$$

where $\Delta\Phi_1 = -2\pi f L_1 (1 - \cos \vartheta_1)/c$, and $\Delta\Phi_2 = -2\pi f L_2 (1 - \cos \vartheta_2)/c$. The frequency dependence of ORF is the product of two sinusoidal oscillations. If one of the angles ϑ_i is fixed, the angular dependence is the same as that of $|\mathcal{P}_i^a(f)|$.

5.2.2. The Near-field Regime

To illustrate the frequency dependence of ORF $\Gamma_{12}(f)$ in the near-field regime, we investigate a simple example by setting $\beta_{12} = 1$ and $L_1 = L_2 = 1$ kpc, $\vartheta_1 = \frac{\pi}{2}$, $\vartheta_2 = \frac{\pi}{4}$. Figure 6 shows $|\Gamma_{12}(f)|$ as a function of f in this case, which is rapidly oscillating with f with some structures. Additionally, the angular dependence of ORF with the angle ϑ_1 (or ϑ_2) in the near-field regime is similar to Figure 4 when the other angle ϑ_2 (or ϑ_1) is fixed.

5.3. The Geometric Factor χ

According to the definition of χ given in Equation (20), χ for a PTA with N_p MSPs where $N_p (\gg 1)$ and PTA MSPs are uniformly distributed on the sky is

$$\chi_f = \sqrt{\int_0^\pi \frac{d\psi}{\pi} \frac{1}{2N_p} \sum_{j=1}^{N_p} |e^{i2\pi f L_j (1 + \hat{\Omega} \cdot \hat{p}_j)/c} - 1|^2 (\mathcal{F}_j^+ + \mathcal{F}_j^-)^2}, \quad (68)$$

¹³ For cases in which they are located in different planes, the conclusions are similar.

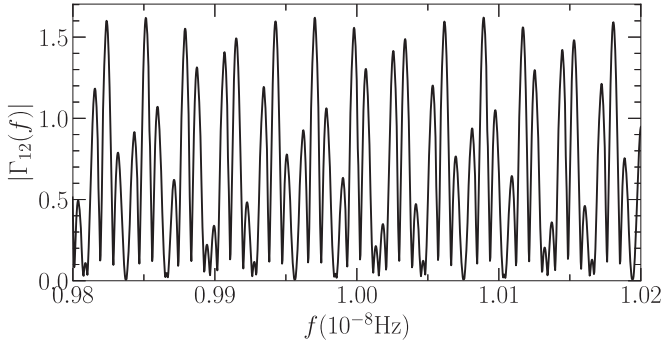


Figure 6. ORF $|\Gamma_{12}(f)|$ (see Section 5.2.2) dependence on f . Here we set $\beta_{12} = 1$, $L_1 = L_2 = 1$ kpc, and $\vartheta_1 = \frac{\pi}{2}$, $\vartheta_2 = \frac{\pi}{4}$.

when the far-field approximation is valid. If not averaging over ψ , we may define χ'_f as

$$\chi'_f \equiv \sqrt{\frac{1}{2N_p} \sum_{j=1}^{N_p} |e^{i2\pi f L_j (1 + \hat{\Omega} \cdot \hat{p}_j)/c} - 1|^2 (\mathcal{F}_j^+ + \mathcal{F}_j^\times)^2}. \quad (69)$$

By averaging over all MSPs, the above equation may be further approximated as

$$\chi_f \simeq \sqrt{\frac{1}{N_p} \sum_{j=1}^{N_p} (\mathcal{F}_j^+ + \mathcal{F}_j^\times)^2}, \quad (70)$$

since $fL/c \gg 1$, and the average of the function $|e^{i\theta} - 1|^2$ over all θ ($\in (0, 2\pi]$) is 2. Moore et al. (2015b) defined χ by approximating the above equation to an average over all directions if the number of MSPs is large and its sky distribution is uniform and set $\iota = 0^\circ$, $\psi = 0^\circ$ ¹⁴

$$\chi'' \simeq \sqrt{\frac{1}{4\pi} \int d^2\hat{\Omega}_{\hat{p}} (\mathcal{F}^+ + \mathcal{F}^\times)^2} = \frac{1}{\sqrt{3}}, \quad (71)$$

where $d^2\hat{\Omega}_{\hat{p}}$ is the solid angle corresponding to pulsar positions.

For individual sources, the inclination angle ι_E can be any value. To estimate the average S/N, we define the mean $\bar{\chi}_f$ by averaging χ_f on all possible ι_E ,

$$\bar{\chi}_f \equiv \sqrt{\int_{-1}^1 \frac{d \cos \iota}{2} \chi_f^2(\iota)} \approx 0.365, \quad (72)$$

in which case, $\iota = \iota_E$.

In the near-field regime, we can also define

$$\chi_n \equiv \sqrt{\int_0^\pi \frac{d\psi_E}{\pi} \frac{1}{2N_p} \sum_{j=1}^{N_p} |\mathcal{P}_j^+(f) + \mathcal{P}_j^\times(f)|^2}, \quad (73)$$

which may be also approximated as

$$\chi_n \simeq \sqrt{\int_0^\pi \frac{d\psi_E}{\pi} \int \frac{d^2\hat{\Omega}_{\hat{p}}}{8\pi} |\mathcal{P}^+(f) + \mathcal{P}^\times(f)|^2}, \quad (74)$$

by averaging over the whole sky.

¹⁴ The misprint in Equation (11) in Moore et al. (2015b) is corrected and

$$\chi \simeq \sqrt{\int_{\phi=0}^{2\pi} \int_{\theta=0}^\pi \frac{\sin \theta d\theta d\phi}{4\pi} \left(\frac{1}{2} \frac{\hat{p}_i \hat{p}_j (A^+ H_{ij}^+ + A^\times H_{ij}^\times)}{1 + \hat{\Omega} \cdot \hat{p}} \right)^2} = \frac{1}{\sqrt{3}}.$$

For individual sources, the inclination angle ι_E can be any value. To estimate the average S/N, we can also define the mean $\bar{\chi}_n$ by averaging χ_n on all possible ι_E ,

$$\bar{\chi}_n = \sqrt{\int_{-1}^1 \frac{d \cos \iota_E}{2} \int_0^\pi \frac{d\psi_E}{\pi} \int \frac{d^2\hat{\Omega}_{\hat{p}}}{8\pi} |\mathcal{P}^+(f) + \mathcal{P}^\times(f)|^2}. \quad (75)$$

The calculation details and the orientation dependence of χ can be seen in Appendix B. We adopt $\bar{\chi}_n$ in our S/N calculation and compare the difference of $\bar{\chi}_n$ and $\bar{\chi}_f$ as follows.

If adopting the optimal templates for detection, the differences of S/N estimations between the near-field regime cases and those adopting the far-field approximation are at least partly represented by the differences in $\bar{\chi}$. It is worth noting here that a low value of FF reflects the S/N decline due to the utilization of inaccurate GW templates, while the variation of $\bar{\chi}$ reflects the S/N change due to the geometric configuration of different PTA pulsars from the configuration in the far-field approximation (which is separated from the effects of inaccurate GW templates). The $\bar{\chi}$ represents the average response of stochastic uniform distributed PTA to GW source. We illustrate the dependence of such differences on the distance of GW sources below. We first consider a GW source located at the GC ($r = 8$ kpc) with a typical PTA frequency $f = 10^{-8}$ Hz (or 10^{-7} Hz; the χ value is independent of f), with which the distance between MSP and Earth L is much larger than the GW wavelength $\lambda_{\text{GW}} \sim 1 - 0.1$ pc. We calculate $\bar{\chi}_n$ and $\bar{\chi}_f$ according to Equations (73) and (68) for the near-field and far-field regimes, respectively, for PTAs with different typical pulsar distance L . (The averaged $\bar{\chi}_f \simeq 0.365$.) Figure 7 shows the resulting $\bar{\chi}_n$ (solid lines, left panel), $\bar{\chi}_f$ (black dashed line), and their ratio versus pulsar distance L with a fixed source distance r , either 8 kpc (GC distance) or 50 kpc (LMC distance), and also $\bar{\chi}_n$ (solid lines, right panel) as a function of the GW source distance r , with a fixed MSP distance L , either 2 kpc or 10 kpc. According to this Figure and our calculation results, a number of conclusions can be summarized as follows:

1. $\bar{\chi}_n$ is roughly 0.365 when L is a factor of about four times smaller than r (or $L \ll r$), which is exactly the case that the far-field approximation works. $\bar{\chi}_n$ begins to increase when L is larger and reaches a maximum value when $L \simeq r$, then $\bar{\chi}_n$ declines rapidly to a value of $\simeq 0.26$ when L becomes larger than r and this value is even less than $\bar{\chi}_f$ (see Figure 7). The change of $\bar{\chi}_n$ with L suggests that the near-field effect is significant when L is comparable to or larger than the GW source distance.
2. The large value of $\bar{\chi}_n$ at $L \simeq r$ is mainly due to the contribution from PTA pulsars with small ϑ . For small ϑ , $\bar{\chi}_n$ can be inversely proportional to ϑ , as seen from Equation (E6) in Appendix E.
3. When $L \gg r$ or $r \ll L$, $\bar{\chi}_n$ becomes flat and can be smaller than $\bar{\chi}_f$ as shown in Figure 7. The main reason for this is as follows. The contribution from those PTA pulsars with small ϑ becomes small due to the responses in the pulses of a pulsar to the GW signals at the near side of the pulse path being (partly) canceled by those at the far side of the pulse path.
4. Both $\bar{\chi}_n$ and $\bar{\chi}_f$ do not depend on the GW frequency. The reason for this is that f is only included in the phase factor of $\mathcal{P}^a(f)$, which is averaged over ϑ of many different MSPs in the calculations of $\bar{\chi}$.

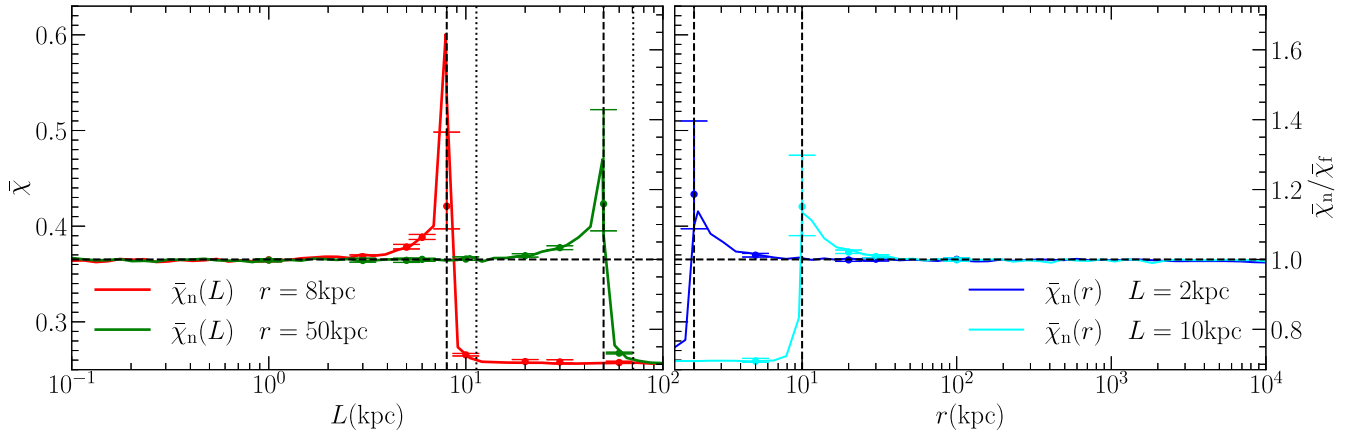


Figure 7. Left panel: $\bar{\chi}(L)$: $\bar{\chi}$ as a function of the PTA pulsar distance L (Equation (75)) in the near-field regime for a source at a distance of $r = 8$ kpc (red solid line) and $r = 50$ kpc (green solid line), respectively. Right panel: $\bar{\chi}_n/\bar{\chi}_f$: $\bar{\chi}_n/\bar{\chi}_f$ as a function of the GW source distance r in the near-field regimes for a PTA obtained by averaging results from 50,000 different parameters sets, with pulsars randomly distributed on sky at a distance of $L = 2$ kpc (blue solid line) and $L = 10$ kpc (cyan solid line), respectively. The black dashed horizontal line shows $\bar{\chi}$ obtained by adopting the far-field approximation, i.e., $\bar{\chi}_f = 0.365$. The ratio $\bar{\chi}_n/\bar{\chi}_f$ as a function of L is indicated by the right vertical axis, where averaged $\bar{\chi}_f \approx 0.365$. The top and bottom horizontal axes indicate source distance r and pulsar distance L , respectively. Different realizations for the sky locations of the PTA pulsars may result in different $\bar{\chi}_n$, especially when L is comparable to r . To illustrate this, the uncertainties due to different realizations for some cases with fixed r but different L and with fixed L but different r are shown in both the left and right panels (solid circles with error bars). The solid circles and its associated error bars represent the median and the 16%–84% range of $\bar{\chi}_n$ obtained from 50 realizations of the PTA pulsar sky locations (see Section 5.2.2).

One should keep in mind that the $\bar{\chi}$ here is a mean geometric factor averaged over PTA MSPs. In real observations, the exact near-field effect depends on the properties of those PTA MSPs and the position of the source.

6. Applications

In this Section, we apply the theoretical framework presented in Section 4 to estimate S/Ns of some hypothetical MBBHs in the GC and the center of LMC, monitored by current and future PTAs, and thus check whether they can be detected by PTAs, if any.

6.1. Monochromatic GW Signals

The GW from MBBHs in the PTA band is almost monochromatic since the frequency variation rate is negligible. In this case, the GW strain can be approximated as in Equations (4) and (5), where the GW phase $\Phi(t) = 2\pi f_0 t$, GW amplitude $h_0 = 4(G\mathcal{M}_c)^{2/3}(\pi f_0)^{2/3}/c^4 r$ with $\mathcal{M}_c = (M_{\bullet 1}M_{\bullet 2})^{3/5}/M_{\bullet}^{1/5}$, $M_{\bullet} = M_{\bullet 1} + M_{\bullet 2}$, $M_{\bullet 1}$ and $M_{\bullet 2}$ are the masses of two components. The Fourier transforms of the GW strains are

$$\tilde{h}_{+,o}(f) = h_0(f_0)(\delta(f - f_0) + \delta(f + f_0))/2, \quad (76)$$

$$\tilde{h}_{\times,o}(f) = h_0(f_0)(\delta(f - f_0) - \delta(f + f_0))/2. \quad (77)$$

Only the half with $f > 0$ of the frequency spectrum appears in the integral for estimating S/N (see Equations (85) and (87) below); thus, the rms strain is

$$|\tilde{h}_{a,o}(f)| = \frac{h_0(f_0)\delta(f - f_0)}{\sqrt{2}}. \quad (78)$$

In reality, the total observation time T cannot be infinite, and thus $\delta(f)$ should be replaced by $\delta_T(f) = \sin(\pi f T)/(\pi f)$ (Moore et al. 2015b).

Figure 8 shows $|\tilde{h}_o(f)|$ and $|\tilde{z}(f)|$ obtained for an example MBBH with $h_0 = 10^{-15}$ at $f_0 = 10^{-8}$ Hz, according to Equation (13) by assuming $\vartheta = \pi/2$, $L = 1$ kpc, $r = 8$ kpc, and $\iota_E = \psi_E = 0$ (see Section 5.1.2). In this case, $\mathcal{P}^\times(f) = 0$;

therefore,

$$|\tilde{z}(f)| = |\mathcal{P}^+(f)| |\tilde{h}_{+,o}(f)|. \quad (79)$$

The frequency spectrum of redshift $|\tilde{z}(f)|$ is a modulated GW signal spectrum due to the oscillation of $\mathcal{P}^a(f)$. This modulation is important in the matched-filtering. If the far-field approximation is adopted and only the Earth term is considered, the waveform template is not modulated as it should be, which may lead to a significant decline of S/N estimated for nearby GW sources and large errors in parameter estimations of the GW system. For the SKA-PTA, we obtain $\text{FF} = 0.758$ if the un-modulated $|\tilde{h}_{a,o}(f)|$ is adopted to match $|\tilde{z}(f)|$. This demonstrates the importance of the near-field effect; otherwise, it would lead to S/N underestimation with a factor $\sqrt{\text{FF}} \approx 0.87$.

6.2. PTA Noises

The noises for PTA detection of individual GW sources can be divided into three main parts: the red noise, the shot noise, and the confusion from the GWB (Rosado et al. 2015; Goldstein et al. 2019). Here we do not consider the (intrinsic) red noises of pulsars though they are practically important. The main reason for this is that there are larger uncertainties in these red noises and their behavior is currently not fully understood (e.g., Lentati et al. 2016; Goncharov et al. 2020). Generally, the PSD of the GWB strain contributed by the shot noise is described as (Creighton & Anderson 2011)

$$S_{n,s}(f) = 8\pi^2 \sigma^2 f^2 \Delta t, \quad (80)$$

where σ is the rms of the pulsar timing noise, and Δt is the mean cadence of the PTA observations. The strain of GWB due to GW radiation from numerous distant MBBHs can be described as (Chen et al. 2020, c.f., Sampson et al. 2015)

$$h_b = \mathcal{A} \frac{(f/1\text{yr}^{-1})^{-2/3}}{[1 + (f_{\text{bend}}/f)^{\kappa_{\text{gw}} \gamma_{\text{gw}}}]^{1/(2\gamma_{\text{gw}})}}. \quad (81)$$

We adopt $\log \mathcal{A} \sim -15.70$, $f_{\text{bend}} = 2.45 \times 10^{-10}$ Hz, $\kappa_{\text{gw}} = 3.74$, and $\gamma_{\text{gw}} = 0.19$, which are the median values for the GWB

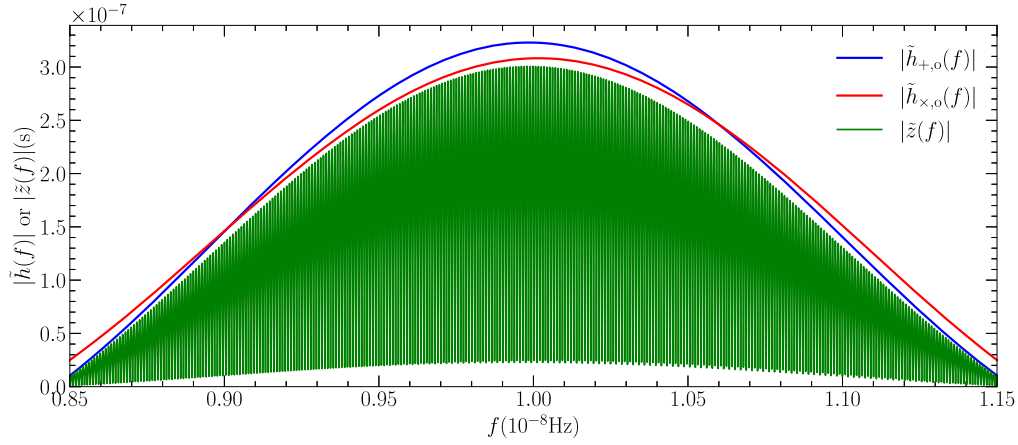


Figure 8. $|\tilde{h}_{a,o}(f)|$ (Equation (78)) and $|\tilde{z}(f)|$ (Equation (79)) (both in units of seconds) obtained from the fast Fourier transformation of a monochromatic GW source located at $r = 8$ kpc with amplitude $h_0 = 10^{-15}$ and frequency $f = 10^{-8}$ Hz in the frequency domain “observed” by a PTA with $L = 1$ kpc over a time span of $T = 20$ yr. The $|\tilde{z}(f)|$ shown here is a modulated GW signal spectrum. This modulation occurs only when the pulsar term (in the term of $\mathcal{P}^+(f)$ in Equation (79)) is considered and the results obtained in the near-field case are different from those obtained in the case adopting the far-field approximation. See Section 6.1 for details.

predictions in Chen et al. (2020). The total noise for individual PTA sources is then

$$S_n(f) = S_{n,s} + \frac{h_b^2}{f}, \quad (82)$$

or

$$h_n(f) = \sqrt{f S_{n,s} + h_b^2}. \quad (83)$$

In the calculation of the S/N in this paper, we consider the GWB as a source of noise. It is also possible to only consider the shot noise to give optimistic S/N estimates after the GWB is well modeled and extracted from the PTA data. For the cross-correlation method, both the GWB and signal from an individual source are cross-correlated, though they have different spectra. It is necessary to distinguish them from each other by using the matched-filtering method to extract individual signals and power-law modeling of the GWB. Combining the cross-correlation and matched-filtering methods together, it is possible to obtain even higher S/Ns for single sources.

6.3. S/N

We further derive the formulas to estimate the S/N for monochromatic GW sources monitored by a coherent network of PTA within a limited time duration (T) as follows.

1. Matched-filtering Method: the expected S/N can be roughly estimated as (combining Equations (50) and (78)),

$$\begin{aligned} \varrho^2 &= N_p \int_0^\infty df \frac{2\chi^2 h_0^2(f_0) \delta_T^2(f - f_0)}{S_n(f)}, \\ &\approx N_p \frac{2\chi^2 h_0^2(f_0) T}{S_n(f_0)}, \end{aligned} \quad (84)$$

where $\delta_T(f) = \sin(\pi f T) / (\pi f)$ and $\delta_T(0) = T$ (Moore et al. 2015b) or equivalently,

$$\varrho^2 \approx N_p \frac{\chi^2 h_c^2}{h_n^2}, \quad (85)$$

where the characteristic strain $h_c = h_0 \sqrt{2fT}$, and $h_n^2 = f S_n$ (see Moore et al. 2015a).

2. Cross-correlation Method: the expected S/N can be roughly estimated as (combining Equations (55) and (78))

$$\begin{aligned} \varrho^2 &= \frac{N_p(N_p - 1)}{T} \int_0^\infty df \frac{\chi^4 h_0^4(f_0) \delta_T^4(f - f_0)}{S_n^2(f)} \\ &\approx N_p(N_p - 1) \frac{\chi^4 h_0^4(f_0) T^2}{S_n^2(f_0)}, \end{aligned} \quad (86)$$

or equivalently,

$$\varrho^2 \approx \frac{N_p(N_p - 1)}{4} \frac{\chi^4 h_c^4}{h_n^4}. \quad (87)$$

Once the properties of a PTA (σ , Δt , N_p) and a GW source (h_0 and f_0) are given, we can estimate its expected S/Ns according to Equations (85) and (87). Note that the cross-correlation method usually results in a substantially higher S/N than that from the matched-filtering method if the S/N of one detection is higher than a threshold value of three according to the above two equations.

Table 1 lists the (assumed) properties of a few current PTAs (EPTA/NANOGrav/PPTA, and IPTA), the CPTA (Lee 2016), and SKA-PTA (Sesana & Vecchio 2010; Moore et al. 2015a). We further note that a population of pulsars may exist within 1 pc from the GC and SKA may discover up to 100 pulsars in the vicinity of Sgr A* according to recent model predictions (e.g., Pfahl & Loeb 2004; Zhang et al. 2014). If some of those pulsars are stable MSPs, they may be monitored to form a special PTA (denoted as GC-PTA; see also Table 1), which may be useful in detecting the nanohertz GW signals from the GC (see Kocsis et al. 2012).

It is worth noting here that our S/N formulas are somewhat different from those in Huerta et al. (2015) and Moore et al. (2015b).

First, the PSD S_n defined by Equation (82) (see also Creighton & Anderson 2011) is different from that defined in these two works. In Moore et al. (2015b), the adopted shot noise $S_n = 2\sigma^2 \Delta t$ is the PSD of the timing residuals, while $S_n = 24\pi^2 \Delta t \sigma^2 f^2$ in Huerta et al. (2015) (from Thrane & Romano 2013) is the PSD of

the GW strain. The shot noise (see Equation (80)) we adopt is similar to Huerta et al. (2015) and Thrane & Romano (2013), but with a different coefficient of $8\pi^2$. The influence from the GWB is included in our PSD S_n , but not in Huerta et al. (2015) and Thrane & Romano (2013). Second, we do not make approximations like those in Moore et al. (2015b), in which the power of four in their Equation (12) was replaced by two, and then extended to the low- and high-frequency limits. We keep the accurate expression to calculate sensitivity curves numerically. Third, the dependence of S/N ϱ on N_p in this paper is a little different from that in Huerta et al. (2015). For simple superposition of coherent networks (such as Wang et al. 2014; Rosado et al. 2015; Wang et al. 2015), we have $\varrho^2 \propto N_p h_c^2 / h_n^2$; while if the cross-correlation method was adopted for each pulsar pairs, we have $\varrho^2 \propto N_p(N_p - 1)h_c^4 / h_n^4$ (Moore et al. 2015b). However, Huerta et al. (2015) obtained $\varrho^2 \propto N_p(N_p - 1)h_c^2 / h_n^2$, which may overestimate the sensitivity of a PTA when N_p is high if setting $\varrho \equiv 1$ to define the PTA sensitivity. We also note here that the difference between the S/Ns given by the matched-filtering method and the cross-correlation method results partly from the different definitions of the signals. The former is defined to be linear in the GW strain amplitude, while the latter as a quantity quadratic in the strain amplitude or linear in the GW power, which is the difference between these two methods (see also Maggiore 2008).

6.4. Hypothetical GC MBBH

We assume that there exists a circular intermediate mass BH(IMBH)-MBH binary in the GC ($r = 8$ kpc) with a total mass of $M_{\bullet\bullet} = 4.4 \times 10^6 M_\odot$ as given by observations (e.g., Schödel et al. 2003; Genzel et al. 2010; Boehle et al. 2016; Gillessen et al. 2017; Do et al. 2019), and the mass ratio is $q = M_{\bullet,2}/M_{\bullet,1}$, though the probability for the existence of an MBBH with large q (e.g., > 0.001) in the GC may be little (see Abuter et al. 2020). We also assume that the GW frequency is either $f_0 = 10^{-8}$, 3×10^{-8} , or 10^{-7} Hz, in the PTA band. Therefore, the GW strain and characteristic GW strain are

$$h_0 \approx 8.2 \times 10^{-15} \frac{q}{(1+q)^2} \left(\frac{f_0}{10^{-8} \text{ Hz}} \right)^{\frac{2}{3}} \times \left(\frac{r}{8 \text{ kpc}} \right)^{-1} \left(\frac{M_{\bullet\bullet}}{4.4 \times 10^6 M_\odot} \right)^{\frac{5}{3}}, \quad (88)$$

and

$$h_c \approx 2.0 \times 10^{-14} \frac{q}{(1+q)^2} \left(\frac{f_0}{10^{-8} \text{ Hz}} \right)^{\frac{7}{6}} \times \left(\frac{T}{10 \text{ yr}} \right)^{\frac{1}{2}} \left(\frac{r}{8 \text{ kpc}} \right)^{-1} \left(\frac{M_{\bullet\bullet}}{4.4 \times 10^6 M_\odot} \right)^{\frac{5}{3}}, \quad (89)$$

respectively. Adopting the mean of the distances of pulsars (L) for EPTA/NANOGrav/PPTA, IPTA, CPTA, and SKA-PTA as ≈ 2 kpc (Manchester et al. 2005), $\bar{\chi}_n \sim 0.368$ (see Figure 7), is almost the same as that given by the far-field approximation $\bar{\chi}_f$. We then estimate the S/Ns for these different PTAs as listed in Table 1. It appears that the current PTAs (NANOGrav/EPTA/PPTA) are not likely to detect the GW signal with $f \sim 10^{-8} - 10^{-7}$ Hz from a hypothetical MBBH in the GC with $q \sim 0.01$ or less.

If the IPTA can include more pulsars (e.g., $N_p = 200$), observe more frequently (e.g., $\Delta t = 0.01$ yr) with a higher timing precision ($\sigma_t = 30$ ns), like the row for IPTA^{opt} in Table 1, such GW signals may be detectable in the frequency range of $f \sim 10^{-8} - 10^{-7}$ Hz with $S/N \varrho > 3$. The CPTA may be only able to detect the GW signal from a hypothetical MBBH with q as small as ~ 0.01 at $f \sim 3 \times 10^{-8}$ Hz with $\varrho > 3$. If the mass ratio $q \ll 0.01$, the IPTA^{opt} and CPTA are not expected to detect such GW sources with substantially large S/Ns, but the SKA-PTA may be able to detect the GW signal from a hypothetical MBBH with q as small as $\lesssim 0.001$ with an S/N $\varrho \gtrsim 3$.

We also estimate the expected S/Ns for hypothetical MBBHs in the GC monitored by a possible PTA composed of MSPs close to it (see, e.g., Kocsis et al. 2012). The properties of such a GC-PTA are assumed to be those in the ‘‘GC-PTA’’ row listed in Table 1. From Equation (E6), we have

$$\bar{\chi} \approx 2.92 \times 10^3 \left(\frac{r_p}{1 \text{ pc}} \right)^{-1}. \quad (90)$$

The obtained S/Ns via the GC-PTA are high enough even if only 10 MSPs with timing noises of 100 ns can be detected and applied. With such a GC-PTA, even the GW signals from a BH with mass down to several hundred times of solar masses rotating around the central MBH may be also detectable. This suggests that MSPs, if existing in the vicinity of the GC MBH, should be useful in detecting/constraining low-frequency GWs emitted from IMBHs or even stellar-mass BHs rotating around the GC MBH.

6.5. LMC

An MBH with $M_{\bullet,1} \approx 2 \times 10^4 M_\odot$ is suggested to exist in the center of the LMC (Boyce et al. 2017). There was also tentative evidence for the existence of an MBBH in the LMC center, e.g., hypervelocity star ejected from the LMC (e.g., Erkal et al. 2019). Suppose there exists another IMBH with mass $M_{\bullet,2} \approx 2 \times 10^3 M_\odot$ rotating around the central MBH M_1 , and the GW emission from such a binary system is at a frequency either of $f_0 \approx 10^{-8}$, 3×10^{-8} , or 10^{-7} Hz. The distance from the LMC to Earth is about $r = 49.97$ kpc (Pietrzyński et al. 2013). Thus, the GW strain received at the Earth can be obtained from Equations (88) and (89). In this case, it is difficult to detect the GW signal by current PTAs and even future SKA-PTA. However, if the hypothetical MBBH is monitored via a PTA composed of MSPs at the LMC center as listed in Table 1, then

$$\bar{\chi} \approx 1.82 \times 10^4 \left(\frac{r_p}{1 \text{ pc}} \right)^{-1}. \quad (91)$$

As shown in Table 1 (the last two rows), as long as 20 MSPs in the center of LMC with $r_p \sim 1$ pc can be detected and applied to form a PTA, the GW signal can be detected with $S/N \approx 4-15$; if only five MSPs at $r_p \sim 0.1$ pc, the GW signal can be detected with an $S/N \approx 20-340$. Note that 59.7 kpc is the farthest distance the pulsar is away from Earth in the pulsar catalog¹⁵ (Manchester et al. 2005), and 21 pulsars in the LMC have been discovered (Cordes & Chatterjee 2019). It is possible that many MSPs in the LMC may be detected in the SKA era.

¹⁵ <http://www.atnf.csiro.au/people/pulsar/psrcat>

However, it would be a challenge to get the high-precision timing demanded by the PTA to detect GWs.

7. Conclusions

We investigate the detection of GWs emitted from nearby MBBHs via PTAs and introduce a general theoretical framework to study the near-field effect on detecting these MBBHs by utilizing the standard matched-filtering method and the cross-correlation method. We find that the traditional plane-wave approximation adopted for faraway GW sources is not valid in the cases for detecting MBBHs at distances comparable to or not much larger than the distances of PTA pulsars. In this framework, we derive new and general expressions for some physical quantities, such as the geometric factor χ , the ORF, and the S/N estimators for both the matched-filtering and the cross-correlation detection methods. Our main conclusions are summarized as follows.

1. The near-field effect is significant in extracting GW signals from nearby MBBHs via PTA observations, as the matched-filtering is sensitive to the exact GW waveform in the frequency domain. For the detection of such nearby MBBHs, an appropriate modification should be made on the GW templates used in the far-field approximation; otherwise, it will lead to an underestimate of the S/N (e.g., up to a factor of 1.36 for an MBBH in the GC; see Figure 5) and further increase uncertainties in the estimation of the system parameters.
2. Combining the small-scale spiky features of the angular distribution of the response of PTA and the GW parallax effects due to the curvature of the wavefronts of GWs, the spatial locations of nearby GW sources may be determined to high precision (e.g., $\lesssim 1^\circ$ as seen from Figure 4), and thus the degeneracy between GW frequency and MSP distances may also be broken in the near-field regime.
3. MSPs in the GC, if any, will be powerful probes to nanohertz GWs emitted from the GC. If some stable MSPs located around the GC are discovered in the future, the GW signal from an MBBH (if any) in the GC can be detected with a high S/N even if only several suitable stable MSPs are observed. Similarly, a PTA composed of some stable MSPs in the LMC can also be used to detect the GW signal from an MBBH (if any) in the LMC.
4. For most known MSPs ($L \sim 1\text{--}2$ kpc) currently adopted in PTAs, the near-field effect is significant if the MBBH distance $r \lesssim 30$ Mpc in actual detection. Many galaxies are located within this distance, and they may have MBBHs in their centers as possible GW sources for PTAs (Schutz & Ma 2016); therefore, the near-field effect needs to be carefully considered when using PTA to search for such GW sources. If more MSPs with greater distances were adopted in future PTAs, the near-field effect could be significant for MBBHs at even greater distances.
5. The angular correlation between the responses of different pulsars to an isotropic GWB contributed by isotropically distributed nearby sources is similar to the Hellings–Downs curve obtained by the far-field approximation except for the value at $\theta_{12} = 0^\circ$.

For simplicity, in our analysis we have neglected some observational effects, such as high-order effects in real observations like the red noises in pulsar timings (Rosado et al. 2015; Goncharov et al. 2020) and the post-Newtonian

effects (Kocsis et al. 2012). These effects should be considered carefully when extracting GW signals of MBBHs from the TOA data series of PTAs.

We thank the referee for helpful comments and suggestions. This work is partly supported by the National SKA Program of China (grant No. 2020SKA0120101), National Key Program for Science and Technology Research and Development (grant Nos. 2020YFC2201400 and 2016YFA0400703/4), the National Natural Science Foundation of China (grant Nos. 11721303, 11873056, 11991052, 12173001, and 11690024), and the Strategic Priority Program of the Chinese Academy of Sciences (grant No. XDB 23040100).

Appendix A Two Coordinate Systems

In general cases, the GW propagation directions $\hat{\Omega}$ are different at different Q (see Figure 1). We can define two kinds of coordinate systems. One is such a frame rotating with $\hat{\Omega}$ in the pulsar-Earth-GW source plane, and $(\hat{e}_1, \hat{e}_2, \hat{\Omega})$ are taken as the x -, y -, and z -axis bases. Here \hat{e}_1 is perpendicular to the pulsar-Earth-GW source plane, and \hat{e}_2 is a unit vector in the pulsar-Earth-GW source plane perpendicular to $\hat{\Omega}$. This coordinate system is denoted as the $(\hat{e}_1, \hat{e}_2, \hat{\Omega})$ system. Rotating this coordinate system by a polarization angle ψ , we can obtain the coordinate system in traverse traceless gauge. It is convenient to calculate the antenna pattern function in such a coordinate system because $\hat{e}_1, \hat{e}_2, \hat{\Omega}$ are invariant, though the pulsar direction $\hat{p} = (0, \sin \gamma, \cos \gamma)$ does change. In this coordinate system, antenna pattern functions are expressed as

$$F^+(l) = -\frac{\sin^2 \gamma}{2(1 + \cos \gamma)} = -\frac{1 - \cos \gamma}{2}, \quad (\text{A1})$$

$$F^\times(l) = 0. \quad (\text{A2})$$

Another one is the fixed coordinate system relative to the observer's sky. We choose $(\hat{e}_1, \hat{e}_{2,E}, \hat{\Omega}_E)$ at Earth as the x -, y -, and z -axis bases. We denote it as the $(\hat{e}_1, \hat{e}_{2,E}, \hat{\Omega}_E)$ coordinate system. In this coordinate system, the pulsar direction $\hat{p} = (0, \sin \vartheta, -\cos \vartheta)$ and \hat{e}_1 does not change; however, \hat{e}_2 and $\hat{\Omega}$ change with Q and $\hat{e}_2 = (0, \cos \zeta, -\sin \zeta)$, $\hat{\Omega} = (0, \sin \zeta, \cos \zeta)$. It is convenient to transfer this frame to the celestial coordinates. We can also obtain the same antenna pattern function in this coordinate system, if choosing the same bases. These two coordinate systems are approximately the same in the far-field regime, i.e., the GW source is far away from PTA MSPs.

Appendix B Some Formulas for Calculating χ

According to the geometry illustrated in Figure 1(a) for a general configuration of the GW source, Earth, and PTA MSP, we have

$$r'^2 = l^2 + r^2 - 2lr \cos \vartheta, \quad (\text{B1})$$

$$\cos \gamma = \frac{l - r \cos \vartheta}{\sqrt{l^2 + r^2 - 2lr \cos \vartheta}}, \quad (\text{B2})$$

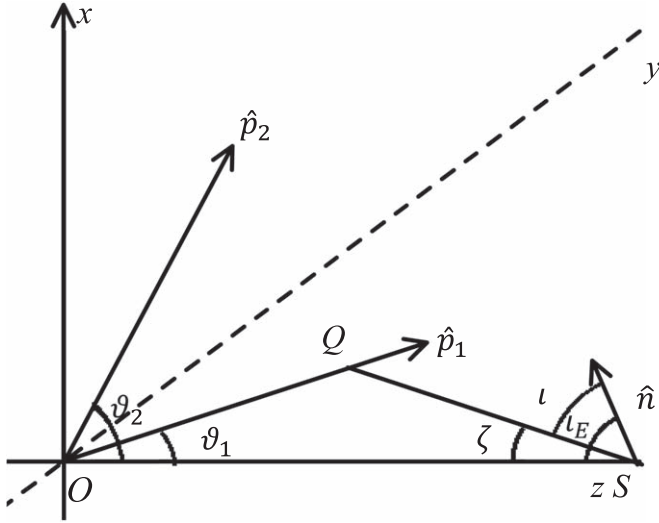


Figure 9. The three-dimensional schematic for the configuration of a GW source and two pulsars, where two pulsars, GW sources (S), and Earth are not located in the same plane; Earth is located at the origin O of coordinate system; and pulsar 1 is located in the plane yOz . It should be noted that the positive direction of the z -axis points to the left.

and

$$\cos \zeta = \frac{r - l \cos \vartheta}{\sqrt{l^2 + r^2 - 2lr \cos \vartheta}}, \quad (\text{B3})$$

where ϑ is the angle between the line of sight to the GW source and that to the pulsar. For a given GW source, r' is a function of l as r and ϑ are fixed.

Since l can be comparable to r , γ and ζ may vary significantly for different points Q along the propagation paths of pulses from pulsars to Earth. If $\iota_E = 0^\circ$, we have $\iota = \zeta$ at any point Q between the Earth and pulsar. Because $\hat{\Omega}$ is always located in the pulsar-Earth-GW source plane, even if $\iota_E \neq 0^\circ$, as long as \hat{n} is in the pulsar-Earth-GW source plane, $\hat{n} \times \hat{\Omega}$ is always parallel to \hat{e}_1 . Thus, we have the polarization angle $\psi = 0$ for any point Q in this case.

For the general case with $\psi_E \neq 0^\circ$ and $\iota_E \neq 0^\circ$ (see Figure 9), we denote the unit normal vector of the BBH orbital plane as \hat{n} . We use ψ_E and ι_E to denote the angle between the pulsar-Earth-GW source plane and \hat{n} - $\hat{\Omega}_E$ plane, and the angle between $\hat{\Omega}_E$ and \hat{n} , respectively. From the spherical law of cosines and sines, we have

$$\hat{n} \cdot \hat{\Omega} = \cos \iota = \cos \zeta \cos \iota_E + \sin \zeta \sin \iota_E \cos \psi_E, \quad (\text{B4})$$

$$\sin \psi = \sin \psi_E \frac{\sin \iota_E}{\sin \iota}, \quad (\text{B5})$$

and

$$\cos \psi = \frac{\cos \iota \cos \zeta - \cos \iota_E}{\sin \iota \sin \zeta}. \quad (\text{B6})$$

For a GW source with fixed ι_E , we can use an average over $\cos \vartheta$ and ψ_E to represent the PTA MSPs that are uniformly distributed in the observer's sky.

To show the orientation dependence of χ with ι_E and ψ_E , we define

$$\chi(\iota_E, \psi_E) = \sqrt{\int \frac{d\hat{\Omega}_{\hat{p}}}{8\pi} |\mathcal{P}^+(f) + \mathcal{P}^\times(f)|^2}. \quad (\text{B7})$$

For illustration, Figure 10 shows $\chi(\iota_E, \psi_E)$ as the function of ι and ψ for an example GW source with distance $r = 8$ kpc monitored by a PTA with $L = 2$ kpc. Here we show the results for the region $\psi \in [0, \pi]$, and the results for the region ψ in $[-\pi, 0]$ have a similar pattern due to the symmetry. The mean value of χ can be given by

$$\bar{\chi} = \sqrt{\int_{-1}^1 \frac{d \cos \iota_E}{2} \int_0^\pi \frac{d\psi_E}{\pi} \int \frac{d\hat{\Omega}_{\hat{p}}}{8\pi} |\mathcal{P}^+(f) + \mathcal{P}^\times(f)|^2}. \quad (\text{B8})$$

Appendix C Celestial Coordinate System

In practice, only the celestial coordinates of pulsars and GW sources are known. These angles need to be expressed in a celestial coordinates system. From the spherical law of cosines, it is easy to obtain

$$\cos \vartheta = \cos \delta \cos \delta_p \cos(\alpha - \alpha_p) + \sin \delta \sin \delta_p$$

(e.g., Wahlquist 1987; Lee et al. 2011; Zhu et al. 2015, 2016), where α and α_p are the R.A.s of the GW source and the pulsar, respectively, and δ and δ_p are the decls. of the GW source and the pulsar, respectively. For convenience, we define that the normal vector \hat{n} of the GW source orbital plane points at a direction (α_n, δ_n) in the celestial sphere. The pulsar (p), GW source (S), and \hat{n} (n) three points in the celestial sphere can form a spherical triangle pSn. Its three sides are given by

$$\widehat{pS} = \vartheta,$$

$$\widehat{Sn} = \arccos(\cos \delta \cos \delta_n \cos(\alpha - \alpha_n) + \sin \delta \sin \delta_n),$$

and

$$\widehat{pn} = \arccos(\cos \delta_n \cos \delta_p \cos(\alpha_n - \alpha_p) + \sin \delta_n \sin \delta_p).$$

We also define the angle at point S between sides \widehat{pS} and \widehat{Sn} of the triangle on the celestial sphere as $\angle pSn$. It is easy to obtain that

$$\cos \angle pSn = \frac{\cos \widehat{pn} - \cos \widehat{Sn} \cos \vartheta}{\sin \widehat{Sn} \sin \vartheta};$$

thus, polarization angle ψ_E can be expressed as $|\psi_E| = \angle pSn$ or $\pi - \angle pSn$.

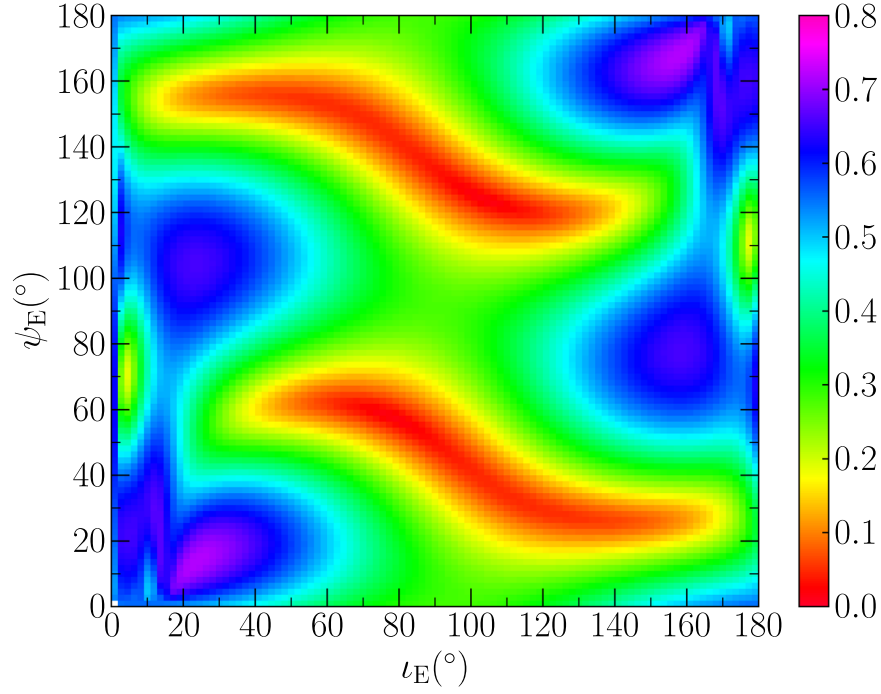


Figure 10. Dependence of $\chi(\iota_E, \psi_E)$ on ι_E and ψ_E for a GW source located at $r = 8$ kpc monitored by a PTA with MSP distances $L = 2$ kpc. Different colors represent different $\chi(\iota_E, \psi_E)$ value as indicated by the right color bar.

Appendix D Waveform Differences for Different Angle ϑ

We have shown the FF and $\delta\hat{\varrho}$ for the case with $\vartheta = \frac{\pi}{2}$ in the main text (see Figure 5). We also calculate the FF and $\delta\hat{\varrho}$ for cases with $\vartheta = \frac{\pi}{4}$ and $\frac{3\pi}{4}$, respectively (see Figure 11). For those cases with $L = 1$ kpc or 2 kpc, the FF and $\delta\hat{\varrho}$ of waveforms of a nearby source at $r = 8$ kpc by adopting the far-field approximation ($r = \infty$) are also summarized in Table 2. Although for different ϑ , the resulting FF and $\delta\hat{\varrho}$ are different,

qualitatively they all suggest that the near-field effect is important for GW sources with distances (i.e., r) not much larger than the PTA pulsar distance (i.e., L), irrespective to the directions of PTA pulsars. Further, we also calculate the maximum distance r (Mpc) that the near-field effect may be important (corresponding to a FF threshold of 0.944 or 0.995) for cases with given PTA pulsar distance L and angle ϑ as listed Table 3. The differences of these maximum distances for cases with different ϑ are about a factor of three or less (see also Figure 11).

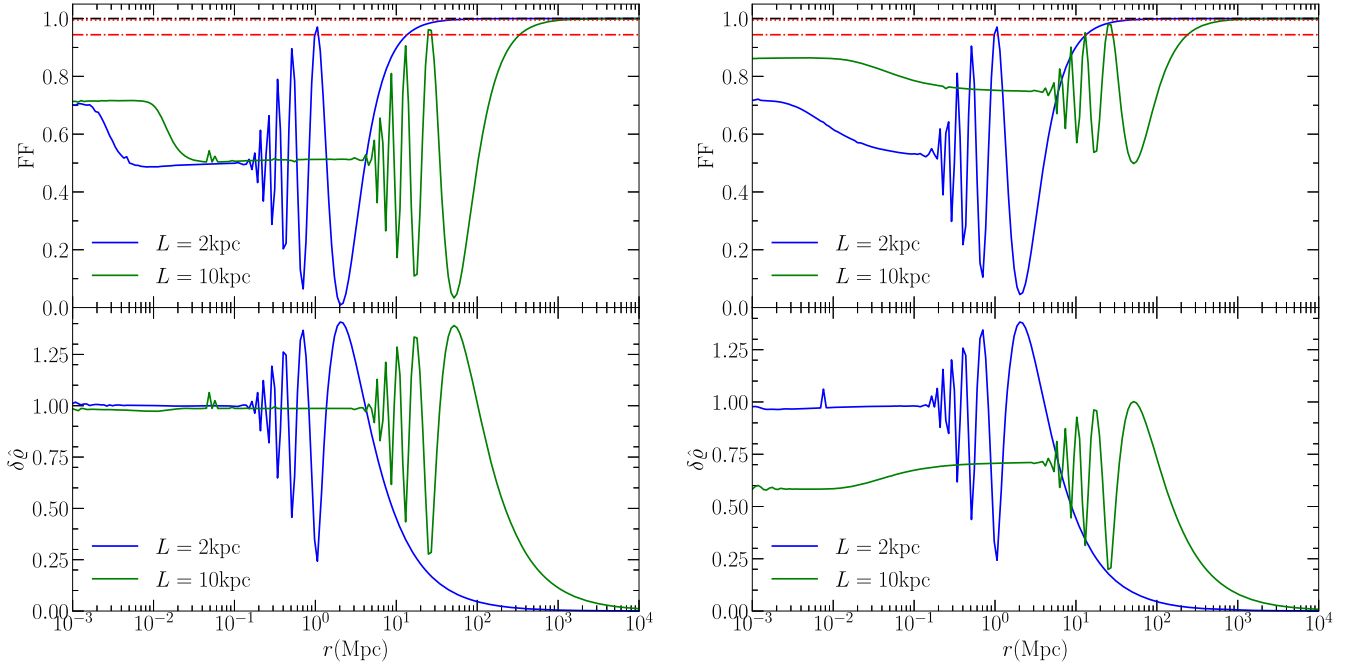


Figure 11. Similar to Figure 5, except for $\vartheta = \frac{\pi}{4}$ in the left panel, and $\vartheta = \frac{3\pi}{4}$ in the right panel.

Table 2

FF (see Equation (62)) and $\delta\hat{\varphi}$ (see Equation (65)) Obtained for Several Cases with Different Choices of ϑ and (L, r)

(L, r) ϑ	(1 kpc, 8 kpc)		(2 kpc, 8 kpc)	
	FF	$\delta\hat{\varphi}$	FF	$\delta\hat{\varphi}$
$\pi/4$	0.490	1.00	0.487	1.00
$\pi/2$	0.537	0.999	0.581	0.993
$3\pi/4$	0.572	0.995	0.635	1.01

Table 3

The Maximum Distance r (Mpc) Obtained for Those Cases with Different Angles ϑ for which FF < FFS (see Definitions of FF and FFS in Equations (62) and (64))

L ϑ	2 kpc		10 kpc	
	FF < 0.944	FF < 0.995	FF < 0.944	FF < 0.995
$\pi/4$	13.7	46.0	338	1140
$\pi/2$	27.1	91.3	572	1933
$3\pi/4$	13.5	45.4	241	821

Appendix E

Pulsars Located around GW Sources

If all PTA MSPs are located around the GW sources, similar to the configuration studied in Kocsis et al. (2012) with all MSPs located in the neighborhood of the GC, it can be also regarded as a special case of the framework considered in Section 2.1. In this case, we have $\vartheta \approx 0$ and $L \approx r$, $r' \approx r - l$, and we define the position vector from the MSP to the GW source as $\vec{r}_p = \vec{r} - L\hat{p}$ and the distance between them is $r_p = |\vec{r}_p|$. Thus Equation (13) can be rewritten as

$$\begin{aligned} \tilde{z}(f) &= \sum_a \tilde{h}_a(f) \int_0^L dl \mathcal{F}^a(l) \frac{d}{dl} \left(\frac{r A_a(l)}{(r-l) A_a(t_E)} \right) \\ &\approx \sum_a \tilde{h}_a(f) \mathcal{F}^a(0) \cdot \left(\frac{r A_a(t_p)}{r_p A_a(t_E)} - 1 \right), \end{aligned} \quad (\text{E1})$$

where the following approximations are adopted,

$$\begin{aligned} \int_0^L dl \mathcal{F}^a(l) \frac{d}{dl} \left(\frac{r A_a(l)}{(r-l) A_a(t_E)} \right) &= \mathcal{F}^a(L) \frac{r A_a(t_p)}{r_p A_a(t_E)} \\ &- \mathcal{F}^a(0) - \int_0^L \frac{r A_a(l)}{(r-l) A_a(t_E)} \frac{d\mathcal{F}^a(l)}{dl} dl, \end{aligned} \quad (\text{E2})$$

and

$$\begin{aligned} \int_0^L \frac{r A_a(l)}{(r-l) A_a(t_E)} \frac{d\mathcal{F}^a(l)}{dl} dl &= \int_0^{L-\epsilon} \frac{r A_a(l)}{(r-l) A_a(t_E)} \frac{d\mathcal{F}^a(l)}{dl} dl \\ &+ \int_{L-\epsilon}^L \frac{r A_a(l)}{(r-l) A_a(t_E)} \frac{d\mathcal{F}^a(l)}{dl} dl \end{aligned} \quad (\text{E3})$$

$$\approx 0 + \frac{r}{r_p} \frac{A_a(t_p)}{A_a(t_E)} [\mathcal{F}^a(L) - \mathcal{F}^a(0)], \quad (\text{E4})$$

where ϵ is a small quantity relative to L but greater than r_p . As $\frac{r}{r-l} \ll \frac{r}{\epsilon} < \frac{r}{r_p}$, the first integral at the right-hand side of Equation (E3) is $< \frac{r}{\epsilon} (\mathcal{F}^a(L - \epsilon) - \mathcal{F}^a(0))$, and $\mathcal{F}^a(l)$ does

not change much in the integration range of l from 0 to $L - \epsilon$. Therefore, the first integral is small compared with the second one and thus can be ignored. For the second integral, we make an approximation $\frac{r}{r-l} \approx \frac{r}{r_p}$ between $L - \epsilon$ and L . Although the variation of ι may be significant between $L - \epsilon$ and L that depends on ψ_E , t_E , r_p , etc. As an approximation, we may use inclination ι_p at MSPs to replace all ι because the integral may be dominated by the contribution from $l \approx L$, and we also adopt the approximation $\mathcal{F}^a(L - \epsilon) \approx \mathcal{F}^a(0)$ to get Equation (E4). Thus

$$\begin{aligned} \mathcal{P}^a(f) &\approx \mathcal{F}^a(0) A_a(t_E) \cdot \left(\frac{r}{r_p} \frac{A_a(t_p)}{A_a(t_E)} - 1 \right) \\ &\approx \mathcal{F}^a A_a(t_p) \frac{r}{r_p}. \end{aligned} \quad (\text{E5})$$

For a GC-PTA, if $r_p \sim 1$ pc, $|\frac{r}{r_p}| \sim 10^3 \gg 1$, and $\frac{A_a(t_p)}{A_a(t_E)} \sim O(1)$ on average, therefore, the pulsar term is much greater than the Earth term, and the Earth term can be ignored. This geometrical configuration is the same as the case considered in Kocsis et al. (2012). The above equations are derived for a single pulsar, and the pulsar term is dominant in Equation (E5). Note that the approximation of taking only one single pulsar term may be inaccurate (see Kocsis et al. 2012), because the combined effect from a PTA should be averaged over all of the different pulsars around the source applied in the PTA. Adopting the general framework presented in Section 2.1 of the present paper, we obtain

$$\bar{\chi} \approx \frac{r}{r_p} \bar{\chi}_f \approx 0.365 \frac{r}{r_p} \quad (\text{E6})$$

by averaging over (ψ_E, t_E) for different pulsars.

Appendix F

Relevant Geometry for Calculations of the Angular Correlation Function in the Near-field Regime

For a pair of PTA pulsars (denoted by $i=1$ and 2, respectively), we set a coordinate system for them so that they are located at $\hat{p}_1 = (0, 0, 1)$ and $\hat{p}_2 = (0, \sin \theta_{12}, \cos \theta_{12})$ with θ_{12} denoting the angle between their directions. We set $-\hat{\Omega}_E = (\sin \theta_{\text{gw}} \cos \phi_{\text{gw}}, \sin \theta_{\text{gw}} \sin \phi_{\text{gw}}, \cos \theta_{\text{gw}})$, $\hat{n} = (\sin \theta_n \cos \phi_n, \sin \theta_n \sin \phi_n, \cos \theta_n)$ where θ_{gw} and ϕ_{gw} represent the polar angle and azimuthal angle of the direction of GW source, and θ_n and ϕ_n represent the polar angle and azimuthal angle of the direction of normal vector \hat{n} of the orbital plane in this coordinate system, respectively. Then we have

$$\cos \iota_E = \hat{\Omega}_E \cdot \hat{n},$$

$$\cos \vartheta_i = -\hat{p}_i \cdot \hat{\Omega}_E,$$

$$\sin \psi_{E,i} = \text{sign}[(\hat{p}_i \times \hat{\Omega}_E) \cdot \hat{n}] \frac{|(\hat{p}_i \times \hat{\Omega}_E) \times (\hat{n} \times \hat{\Omega}_E)|}{|\hat{p}_i \times \hat{\Omega}_E| |\hat{n} \times \hat{\Omega}_E|},$$

$$\cos \psi_{E,i} = \frac{(\hat{p}_i \times \hat{\Omega}_E) \cdot (\hat{n} \times \hat{\Omega}_E)}{|\hat{p}_i \times \hat{\Omega}_E| |\hat{n} \times \hat{\Omega}_E|},$$

for $i=1,2$. Thus, we can transform these angles $(\theta_{12}, \theta_{\text{gw}}, \phi_{\text{gw}}, \theta_n, \phi_n)$ into $(t_E, \psi_{E,i}, \vartheta_i)$ for $i=1,2$. According to Appendix B, we can calculate ι , ψ and so on. For each pulsar i , we can calculate

$\mathcal{P}_i^a(f)$ for $a = +, \times$, once $(\iota_E, \psi_E, \vartheta_i)$, L , and the distances of GW sources r are given. We can then obtain $\bar{\Gamma}_{12}^b(f)$ according to Equation (47). When $\iota_E = \frac{\pi}{2}$, $A_\times = \cos \iota_E = 0$ is a singularity in the numerical integration of Equation (47). To avoid this singularity, we excise $|\cos \iota_E| < 10^{-2}$ part in the calculation. Another way to avoid the singularity is to redefine the ORF as

$$\frac{\beta_{12}^b}{4\pi} \int d^2\hat{n} \int d^2\hat{\Omega}_E \sum_a \mathcal{P}_1^{*a}(f, \hat{\Omega}_E) \mathcal{P}_2^a(f, \hat{\Omega}_E),$$

instead of Equation (47). The resulting ORF shape is also similar to that obtained from Equation (47) except for a normalization difference of ~ 2.5 .

Other than using a spherical triangle relation to obtain ψ as shown in Appendix B, we also have another way to calculate ψ according to vector expressions. If $(\hat{p} \times \hat{\Omega}_E) \cdot \hat{n} > 0$, $\psi \in (0, \pi)$, $\sin \psi > 0$, and $\psi = \text{angle}(\hat{n} \times \hat{\Omega}, \hat{p} \times \hat{\Omega})$, where $\text{angle}(\mathbf{a}, \mathbf{b})$ is a function defined to represent the angle between vectors \mathbf{a} and \mathbf{b} . If $(\hat{p} \times \hat{\Omega}_E) \cdot \hat{n} < 0$, $\psi \in (-\pi, 0)$, $\sin \psi < 0$, and $\psi = \text{angle}(\hat{n} \times \hat{\Omega}, -\hat{p} \times \hat{\Omega}) - \pi$. The coordinates of $\hat{\Omega}$ can be obtained from rotating $\hat{\Omega}_E$ by angle ζ around axis $\hat{p} \times \hat{\Omega}_E$. Then we have

$$\sin \psi_i = \text{sign}[(\hat{p}_i \times \hat{\Omega}) \cdot \hat{n}] \frac{|(\hat{p}_i \times \hat{\Omega}) \times (\hat{n} \times \hat{\Omega})|}{|\hat{p}_i \times \hat{\Omega}| |\hat{n} \times \hat{\Omega}|},$$

$$\cos \psi_i = \frac{(\hat{p}_i \times \hat{\Omega}) \cdot (\hat{n} \times \hat{\Omega})}{|\hat{p}_i \times \hat{\Omega}| |\hat{n} \times \hat{\Omega}|}.$$

ORCID iDs

Xiao Guo (郭潇)  <https://orcid.org/0000-0001-5174-0760>

Youjun Lu (陆由俊)  <https://orcid.org/0000-0002-1310-4664>

Qingjuan Yu (于清娟)  <https://orcid.org/0000-0002-1745-8064>

References

Abuter, R., Amorim, A., Bauböck, M., et al. 2020, *A&A*, **636**, L5
 Ajith, P., Babak, S., Chen, Y., et al. 2008, *PhRvD*, **77**, 104017
 Anholm, M., Ballmer, S., Creighton, J. D. E., Price, L. R., & Siemens, X. 2009, *PhRvD*, **79**, 084030
 Antoniadis, J., Arzoumanian, Z., Babak, S., et al. 2022, *MNRAS*, **510**, 4873
 Apostolatos, T. A., Cutler, C., Sussman, G. J., & Thorne, K. S. 1994, *PhRvD*, **49**, 6274
 Arzoumanian, Z., Brazier, A., Burke-Spolaor, S., et al. 2014, *ApJ*, **794**, 141
 Arzoumanian, Z., Baker, P. T., Blumer, H., et al. 2020, *ApJL*, **905**, L34
 Arzoumanian, Z., Baker, P. T., Blumer, H., et al. 2021a, *ApJL*, **923**, L22
 Arzoumanian, Z., Baker, P. T., Brazier, A., et al. 2021b, *ApJ*, **914**, 121
 Babak, S., & Sesana, A. 2012, *PhRvD*, **85**, 044034
 Begelman, M. C., Blandford, R. D., & Rees, M. J. 1980, *Natur*, **287**, 307
 Blair, D., Ju, L., Zhao, C., et al. 2015, *SCPM*, **58**, 5748
 Boehle, A., Ghez, A. M., Schödel, R., et al. 2016, *ApJ*, **830**, 17
 Boyce, H., Lützendorf, N., van der Marel, R. P., et al. 2017, *ApJ*, **846**, 14
 Brazier, A., Lassus, A., Petiteau, A., et al. 2016, *MNRAS*, **458**, 1267
 Charisi, M., Taylor, S. R., Runnoe, J., Bogdanovic, T., & Trump, J. R. 2022, *MNRAS*, **510**, 5929
 Chen, S., Caballero, R. N., Guo, Y. J., et al. 2021a, *MNRAS*, **508**, 4970
 Chen, Y., Yu, Q., & Lu, Y. 2020, *ApJ*, **897**, 86
 Chen, Z.-C., Yuan, C., & Huang, Q.-G. 2021b, *SCPM*, **64**, 120412
 Cordes, J. M., & Chatterjee, S. 2019, *ARA&A*, **57**, 417

Creighton, J., & Anderson, W. 2011, *Gravitational-Wave Physics and Astronomy: An Introduction to Theory, Experiment and Data Analysis* (Weinheim: Wiley-VCH)
 Deng, X., & Finn, L. S. 2011, *MNRAS*, **414**, 50
 Detweiler, S. 1979, *ApJ*, **234**, 1100
 Do, T., Hees, A., Ghez, A., et al. 2019, *Sci*, **365**, 664
 D'Orazio, D. J., & Loeb, A. 2021, *PhRvD*, **104**, 063015
 Ellis, J. A., Siemens, X., & Creighton, J. D. E. 2012, *ApJ*, **756**, 175
 Erkal, D., Boubert, D., Gualandris, A., Evans, N. W., & Antonini, F. 2019, *MNRAS*, **483**, 2007
 Fang, Y., Chen, X., & Huang, Q.-G. 2019, *ApJ*, **887**, 210
 Genzel, R., Eisenhauer, F., & Gillessen, S. 2010, *RvMP*, **82**, 3121
 Gillessen, S., Plewa, P. M., Eisenhauer, F., et al. 2017, *ApJ*, **837**, 30
 Girma, E., & Loeb, A. 2019, *MNRAS*, **482**, 3669
 Goldstein, J. M., Sesana, A., Holgado, A. M., & Veitch, J. 2019, *MNRAS*, **485**, 248
 Goncharov, B., Shannon, R. M., Reardon, D. J., et al. 2021, *ApJL*, **917**, L19
 Goncharov, B., Zhu, X.-J., & Thrane, E. 2020, *MNRAS*, **497**, 3264
 Gourgoulhon, E., Le Tiec, A., Vincent, F. H., & Warburton, N. 2019, *A&A*, **627**, A92
 Guo, X., & Lu, Y. 2022, *PhRvD*, **106**, 023018
 Hawking, S. W., & Israel, W. 1989, *Three Hundred Years of Gravitation*, Vol. 704 (Cambridge: Cambridge Univ. Press)
 Hellings, R. W., & Downs, G. S. 1983, *ApJL*, **265**, L39
 Huerta, E. A., McWilliams, S. T., Gair, J. R., & Taylor, S. R. 2015, *PhRvD*, **92**, 063010
 Jaranowski, P., Kokkotas, K. D., Królak, A., & Tsevas, G. 1996, *CQGra*, **13**, 1279
 Joshi, B. C., Arumugasamy, P., Bagchi, M., et al. 2018, *JApA*, **39**, 51
 Kocsis, B., Ray, A., & Portegies Zwart, S. 2012, *ApJ*, **752**, 67
 Kramer, M., & Champion, D. J. 2013, *CQGra*, **30**, 224009
 Lazio, T. J. W. 2013, *CQGra*, **30**, 224011
 Lee, K. J. 2016, in ASP Conf. Ser. 502, *Frontiers in Radio Astronomy and FAST Early Sciences Symp.* 2015, ed. L. Qain & D. Li (San Francisco, CA: ASP), 19
 Lee, K. J., Wex, N., Kramer, M., et al. 2011, *MNRAS*, **414**, 3251
 Lentati, L., Shannon, R. M., Coles, W. A., et al. 2016, *MNRAS*, **458**, 2161
 Lindblom, L., Owen, B. J., & Brown, D. A. 2008, *PhRvD*, **78**, 124020
 Maggiore, M. 2008, *Gravitational Waves vol.1 Theory and Experiments* (Oxford: Oxford Univ. Press) <http://gen.lib.rus.ec/book/index.php?md5=ee1879513fb76a776528f459e6fbbc31>
 Manchester, R. N., Hobbs, G., Bailes, M., et al. 2013, *PASA*, **30**, 17
 Manchester, R. N., Hobbs, G. B., Teoh, A., & Hobbs, M. 2005, *AJ*, **129**, 1993
 Manchester, R. N. & IPTA 2013, *CQGra*, **30**, 224010
 McGrath, C., & Creighton, J. 2021, *MNRAS*, **505**, 4531
 McLaughlin, M. A. 2013, *CQGra*, **30**, 224008
 Mingarelli, C. M. 2015, *Gravitational Wave Astrophysics with Pulsar Timing Arrays* (Berlin: Springer) doi:10.1007/978-3-319-18401-2
 Mingarelli, C. M. F., Lazio, T. J. W., Sesana, A., et al. 2017, *NatAs*, **1**, 886
 Moore, C. J., Cole, R. H., & Berry, C. P. L. 2015a, *CQGra*, **32**, 015014
 Moore, C. J., Taylor, S. R., & Gair, J. R. 2015b, *CQGra*, **32**, 055004
 Nan, R., Li, D., Jin, C., et al. 2011, *IJMPD*, **20**, 989
 Perera, B. B. P., DeCesar, M. E., Demorest, P. B., et al. 2019, *MNRAS*, **490**, 4666
 Pfahl, E., & Loeb, A. 2004, *ApJ*, **615**, 253
 Pietrzyński, G., Graczyk, D., Gieren, W., et al. 2013, *Natur*, **495**, 76
 Portegies Zwart, S. F., Baumgardt, H., McMillan, S. L. W., et al. 2006, *ApJ*, **641**, 319
 Ransom, S., Brazier, A., Chatterjee, S., et al. 2019, *BAAS*, **51**, 195
 Robson, T., Cornish, N., & Liu, C. 2019, *CQGra*, **36**, 105011
 Romano, J. D., & Cornish, N. J. 2017, *LRR*, **20**, 2
 Rosado, P. A., Sesana, A., & Gair, J. 2015, *MNRAS*, **451**, 2417
 Sampson, L., Cornish, N. J., & McWilliams, S. T. 2015, *PhRvD*, **91**, 084055
 Sazhin, M. V. 1978, *SvA*, **22**, 36
 Schödel, R., Ott, T., Genzel, R., et al. 2003, *ApJ*, **596**, 1015
 Schutz, K., & Ma, C.-P. 2016, *MNRAS*, **459**, 1737
 Sesana, A. 2013, *CQGra*, **30**, 244009
 Sesana, A., & Vecchio, A. 2010, *CQGra*, **27**, 084016
 Sesana, A., Vecchio, A., & Volonteri, M. 2009, *MNRAS*, **394**, 2255
 Smits, R., Lorimer, D. R., Kramer, M., et al. 2009, *A&A*, **505**, 919
 Takekawa, S., Oka, T., Iwata, Y., Tsujimoto, S., & Nomura, M. 2019, *ApJL*, **871**, L1
 Taylor, S. R., Huerta, E. A., Gair, J. R., & McWilliams, S. T. 2016, *ApJ*, **817**, 70
 Taylor, S. R. 2021, arXiv:2105.13270

- Taylor, S., Burke-Spolaor, S., Baker, P. T., et al. 2019, *BAAS*, **51**, 336
- Thrane, E., & Romano, J. D. 2013, *PhRvD*, **88**, 124032
- Tsuboi, M., Kitamura, Y., Tsutsumi, T., et al. 2017, *ApJL*, **850**, L5
- van Haasteren, R. 2014, *Gravitational Wave Detection and Data Analysis for Pulsar Timing Arrays* (Berlin: Springer)
- Wahlquist, H. 1987, *GReGr*, **19**, 1101
- Wang, Y., & Mohanty, S. D. 2017, *PhRvL*, **118**, 151104
- Wang, Y., Mohanty, S. D., & Jenet, F. A. 2014, *ApJ*, **795**, 96
- Wang, Y., Mohanty, S. D., & Jenet, F. A. 2015, *ApJ*, **815**, 125
- Yu, Q. 2002, *MNRAS*, **331**, 935
- Yu, Q., Lu, Y., & Lin, D. N. C. 2007, *ApJ*, **666**, 919
- Yu, Q., & Tremaine, S. 2003, *ApJ*, **599**, 1129
- Zhang, F., Lu, Y., & Yu, Q. 2014, *ApJ*, **784**, 106
- Zhu, X. J., Hobbs, G., Wen, L., et al. 2014, *MNRAS*, **444**, 3709
- Zhu, X.-J., Wen, L., Hobbs, G., et al. 2015, *MNRAS*, **449**, 1650
- Zhu, X.-J., Wen, L., Xiong, J., et al. 2016, *MNRAS*, **461**, 1317